Alternative splicing of the stress-sensitive regulator CIRBP sharpens the cellular response to bacterial infection

Morgane Corre[1], Volker Boehm[2,3], Vinko Besic[1], Anna Kurowska[1], Anouk Viry[1], Amara Mohammad[4], Catherine Semanaud-Beaufort[4], Morgane Thomas-Chollier[4] and Alice Lebreton[1,5*]

[1] Group Bacterial infection, response & dynamics, Institut de biologie de l'ENS (IBENS), École normale supérieure, CNRS, INSERM, Université PSL, 75005 Paris, France.

[2] Institute for Genetics, University of Cologne, Cologne, Germany.

[3] Center for Molecular Medicine Cologne (CMMC), University of Cologne, Cologne, Germany.

[4] GenomiqueENS, Institut de Biologie de l'ENS (IBENS), École normale supérieure, CNRS, INSERM, Université PSL, 75005 Paris, France.

[5] INRAE, Micalis Institute, 78350 Jouy-en-Josas, France.

[*] For correspondence: alice.lebreton@ens.psl.eu

Abstract

Cell autonomous responses to intracellular bacteria largely depend on gene expression reorganization. To gain isoform-level resolution into these regulations, we combined long- and short-read transcriptomic analysis of the response of intestinal epithelial cells to infection by the foodborne pathogen *Listeria monocytogenes* (*Lm*). Expression of the cellular stress response regulator CIRBP (cold-inducible RNA-binding protein) switched from a canonical transcript to a nonsense-mediated decay-sensitive isoform. Permeation of host cell membranes by bacterial pore-forming toxins such as *Lm*-secreted listeriolysin O drove CIRBP alternative splicing *via* CLK1 inhibition and dephosphorylation of serine/arginine-rich (SR) splicing factors, similarly to a previously reported pathway upon heat stress. Selective repression of canonical CIRBP dampened infection while that of the alternative isoform exacerbated it. Consistently, CIRBP-bound RNA targets were shifted towards stress-relevant transcripts upon infection. CIRBP alternative splicing can thus be generalized as a common response to biotic or abiotic stresses also relevant in the context of bacterial infection.

Keywords

Listeria monocytogenes; CIRBP; stress response; listeriolysin O; alternative splicing; bacterial infection.

Introduction

In a fluctuating environment or upon perturbation of tissue homeostasis, cells can undergo a broad variety of damaging conditions that may impair their integrity and function. In response to the action of damaging agents, stress-sensitive pathways coordinate multiple cellular mechanisms of response that include the control of cell cycle checkpoints, the reallocation of resource between major anabolic and catabolic pathways, the protection against macromolecular damage and scavenging damaged components, the launching of pro-inflammatory responses, or eventually cell death (Fulda et al., 2010; Galluzzi et al., 2018). Among key regulators involved in orchestrating cellular stress responses, CIRBP has been previously described as a central stress-response protein. Although it was initially identified for its role in cold-stress adaptation, it also responds to a variety of other non-physiological challenges such as hypoxia, DNA damage response, glucose deprivation, osmotic, oxidative or heat-stresses (De Leeuw et al., 2007; Zhong and Huang, 2017).

Downstream of stress-sensing, the expression of CIRBP has been shown to be regulated not only in abundance, but also via the production of alternative transcripts (Al-Fageeh and Smales, 2009). Accordingly, 46 splice variants of human CIRBP are currently annotated in the Ensembl database (ENSG00000099622). The mechanisms of CIRBP isoform conversion have been investigated in detail in the context of mild cold- and heat shocks, revealing a fine regulation of CIRBP pre-mRNA splicing into alternative isoforms (Haltenhof et al., 2020; Horii et al., 2019; Neumann et al., 2020). Even a moderate increase in temperature results in the inhibition of the activity of the kinase CLK1, leading to the dephosphorylation of serine/arginine-rich splicing factors (SR proteins). In turn, the loss of activity of SR proteins drives the splicing of CIRBP pre-mRNA in favor of an unstable isoform that is sensitive to the nonsense-mediated decay (NMD) pathway of RNA degradation.

The CIRBP protein itself is activated and migrates to cytoplasmic stress granules, where it regulates a number of cellular pathways, including cell cycle and inflammation, via its RNA binding activity and ability to modulate the stability and translation of its targets (De Leeuw et al., 2007; Lujan et al., 2018; Xia et al., 2012). The modulatory role if CIRBP on inflammation is complex and context-dependent; indeed, while it acts as a mediator of tumor-promoting inflammation, it dampens inflammation in the resolution phase of wound healing (Lujan et al., 2018). It was also reported that

in Huh7 cells from liver hepatoma, viral infections reduced the retention of an intron in the 3' of CIRBP coding sequence (CDS) leading to the loss of a long, cytoplasmic protein-coding isoform (CIRBP-225) (Gokhale et al., 2020). Expression of both this long form of CIRBP and the main, shorter isoform (CIRBP-201), which displays a predominantly nuclear distribution, had a proviral effect. In addition to intracellular roles of CIRBP as a RNA-binding protein, during haemorrhagic shock or sepsis, CIRBP can be released in the circulation, where it acts as a damage-associated molecular pattern that promotes inflammatory responses (Qiang et al., 2013). At least part of the inflammatory effects and tissue injury caused by extracellular CIRBP during sepsis relies on its ability to induce neutrophil extracellular traps (Ode et al., 2019).

While CIRBP functions have been investigated in a number of stress conditions including viral infections and sepsis, its regulation and cellular roles have not been documented in the context of bacterial infections. Yet, bacterial challenges have been reported to provoke various types of stresses that are sensed by host cells (Celli and Tsolis, 2015; Knowles et al., 2021; Rodrigues et al., 2018), including infection by the foodborne pathogen *Listeria monocytogenes*. This facultative intracellular bacterium is responsible for listeriosis in cattle and human, a rare but life-threatening disease in immunocompromised individuals and in the elderly that causes death from meningitis, encephalitis or septic shock (Kammoun et al., 2022). Maternofetal transmission of listeriosis is also a cause of miscarriage or stillbirth during pregnancy, or of invalidating neonatal meningitis. A number of studies have reported that *Lm* infection is accompanied by cellular damages that cause potent cellular stress responses, included the activation of the integrated stress response pathway (Pakos-Zebrucka et al., 2016; Pillich et al., 2015; Shrestha et al., 2012). The major cause of *Lm*-triggered stress to its host cell is due to the permeation of cellular membranes by a cholesterol-dependent cytolysin, listeriolysin O (LLO) (Besic et al., 2020; Gonzalez et al., 2011; Pillich et al., 2012; Tattoli et al., 2013).

Here, by undertaking the transcriptome-wide characterization of alternatively processed transcripts upon infection of intestinal epithelial cells by *Lm* using a combined approach based on the analysis of short- and long-read sequencing of cDNAs, we show that alternative splicing (AS) events alter the expression of a number of cellular genes involved in host RNA processing and post-transcriptional regulation, including splicing factors and CIRBP. We identify that the pore-forming activity of LLO is responsible for CIRBP isoform conversion to an NMD-sensitive transcript, *via* the inhibition of the activity of CLK1 kinase and of SR proteins. We observe an opposite effect on infection of the repression of either CIRBP isoform, and identify variations in the sets of CIRBP targets in infected versus uninfected cells. Altogether, our findings generalize the mechanism of CIRBP-based stress responses to the context of a bacterial infection.

Results

Infection of epithelial cells by *Listeria monocytogenes* alters the mRNA alternative splicing landscape

While quantitative aspects of human gene expression changes upon *Lm* infection have been analyzed in-depth in a number of transcriptomic and translatomic studies (Besic et al., 2020; Eldridge et al., 2020), we sought to explore whether gene expression was also affected at the mRNA isoform level, which could impact the function of protein products by identifying alternative splicing events affecting human transcripts at several time points (0, 2, 5, and 10 h) post-infection (hpi) with *Lm* LL195 strain in the LoVo epithelial cell line of colon adenocarcinoma. To this end, we first re-analyzed short-read RNA sequencing (RNS-seq) data that we had previously generated across the infection time-course (Besic et al., 2020) using MAJIQ, which is optimized for the identification of local splicing variations (LSVs) regardless of isoform-based alignments (Vaquero-Garcia et al., 2016). The high-depth of Illumina sequencing of cDNA fragments allowed a robust detection of statistically-significant changes in the use of splice sites across conditions (Tables S1A to S1C), while long read cDNA sequencing of the same set of samples proved better adapted for qualitative investigation of isoform switches in a selected subset of candidate genes at later stages of investigation, but lacked depth for *bona fide* statistical analysis of isoform switches (Tables S1D to S1F). Relative changes in AS occurrence from one condition to another were quantified as the difference in percent spliced-in (PSI), dubbed delta PSI (dPSI). Whereas almost no change in AS events were detected at 2 hpi and 5 hpi when compared to non-infected (NI) cells (4 and 5 LSVs with over 5% dPSI and 95% probability changing, respectively), a large subset of LSVs (417), spanning over 191 genes, were significantly impacted by *Lm* infection at 10 hpi, with no overall gradual pattern across time-points (Figures 1A and 1B). Gene ontology overrepresentation analysis of genes affected by LSVs at 10 hpi revealed a significant enrichment in functions associated with RNA metabolism, and notably with splicing itself (Figure 1C). Alteration of splicing in SRSF1 to 7, 10 and 11 (Figures 1A, S1A and S1B) is consistent with well characterized auto-regulatory feedback loops that govern the expression of genes encoding SR splicing factors (Lareau et al., 2007; Müller-McNicoll et al., 2019; Risso et al., 2012). Together, these results suggest that AS-based regulations contribute to the fine-tuning of the expression of a subset of human genes in response to *Lm* infection, a number of which can themselves have a role in downstream host gene expression regulation. We then sought to investigate in more detail the alternative isoforms of one of these candidate regulators, the upstream pathways leading to their processing, and their potential downstream role in infection.

Alternative use of 3' exons affects CIRBP expression in infected cells

Among the genes affected by the most robust isoform switches, CIRBP (Cold-inducible RNA binding protein) struck us as worthy of functional investigation. Indeed, the reported roles of CIRBP isoform-based regulation in orchestrating cellular responses to different types of cellular damages prompted us to further document its status upon *Lm* infection. High dPSI and probability of changing for two mutually exclusive LSVs detected by short-read analysis (Figures 1A and 1B) was matched by high up- *versus* down-regulation of isoforms mutually differing in the alternative use of exons 7A versus 7b-8 in long-read RNA-seq analysis (Table S1F, Figures 2A and 2B). Due to incomplete reverse transcription or channeling through nanopores, we noticed that mapping of long-read data to specific isoforms of CIRBP suffered from ambiguities for variants that differed only in their 5'-ends. Therefore, we grouped, among the 46 splice variants that are currently annotated for human CIRBP, those that were detected in our analysis into three main classes of isoforms differing in their body and 3'-end (Figure S2): a dominant protein-coding class containing exon 7a, the most representative of which is ENST00000320936.9, CIRBP-201, that represented 76.7% of CIRBP isoforms in non-infected cells (Table S1G); a class of predicted NMD targets containing exons 7b and 8, the prototype of which being ENST00000586636.5, CIRBP-210 (15.3% of transcripts in non-infected cells); and a third, subdominant class encoding elongated versions of the CIRBP protein, best represented by CIRBP-225 (ENST00000589710.5) (7.9% of CIRBP transcripts in non-infected cells). By 10 hpi, CIRPB expression underwent a 5.8-fold reduction in the abundance of CIRBP-201-like isoforms in profit of a 6.1-fold increase for CIRBP-210-like isoforms, which then represented 69.3% of CIRBP transcripts (Figures 2A and 2B, Table S1G). Although CIRBP-225-like transcripts were also up-regulated 3.5-fold at 10 hpi, then reaching 20.9% of total CIRBP transcripts (Table S1G), subsequent investigation focused on the two dominant isoform classes in this study.

These two CIRBP isoform classes essentially differ in their 3' regions, which consist of alternative exons (Figure 2B). The impact of the alternative splicing on the CDS is minimal, giving rise to a 4-amino-acid (AA) shorter protein for CIRBP-210 compared to CIRBP-201, and to the loss of a putative phosphorylation site on a threonine (Yang et al., 2010) (Figure 2C). By contrast, 3'-UTRs differ significantly. Indeed, in CIRBP-210, the presence of an exon-exon junction in the 3'-UTR makes it a target for degradation by NMD (Neumann et al., 2020), which is attested by its sensitivity to the depletion of key NMD factors (data from Boehm et al., 2021). In the LoVo cell line, we confirmed that RNA silencing of the central NMD factor UPF1 resulted in increased CIRBP-210 mRNA abundance and CIRBP protein levels, compared with non-transfected cells (Figures S3A and S3B), indicating that NMD is responsible for CIRBP-210-like isoforms being unstable in non-infected cells.

Upon infection, no general upregulation of annotated human NMD-sensitive transcripts was observed in long-read RNA-seq datasets (Figure S4), ruling out that the increased abundance of CIRBP-210 was due to the impairment of central NMD pathways. This result also implies that, although the production of CIRBP isoforms was shifted in favor of CIRBP-210 in infected cells, this class of transcripts was still sensitive to NMD, and thus less stable than its -201 counterpart. In agreement with CIRBP-210 being less stable than CIRBP-201, the overall mRNA abundance of CIRBP was decreased 1.6-fold at 10 hpi (Figure S1B) (data from Besic et al., 2020). Its coverage in ribosome footprints was reduced 2.8-fold, corresponding to a 1.7-fold drop in translation efficiency. Immunoblotting against CIRBP confirmed that down-regulation of its expression was part of the consequences of *Lm* infection (Figure 2D).

Infection-induced CIRBP isoform switch requires LLO-proficient *Lm* strains

To investigate whether specific virulence properties of *Lm* were mediating the switch in CIRBP isoform usage upon infection, we compared the ability of distinct *Listeria* strains to alter the proportion of CIRBP-201 and -210 isoforms in LoVo cells. Each isoform class was quantified by RT-qPCR using primers specific to alternative terminal exons 7a or 7b-8, then the ratio of CIRBP-210 to -201 relative abundance, normalized to its value in non-infected cells, was compared across conditions (Figure 3A). It should be noted that the selected pairs of exon-specific primers only allow a discrimination between all CIRBP-201-like isoforms on the one hand, CIRBP-210-like isoforms on the other hands, depending on their 3'-UTRs, and cannot discriminate between isoforms within each class. For wild-type (WT) *Lm*, while no significant change was observed at 5 hpi, CIRBP-210 to -201 abundance was increased 1.6-fold at 10 hpi, confirming CIRBP isoform switch. By contrast, neither a 10-h infection with a strain of *Listeria innocua* rendered invasive by carrying *Lm* internalin gene *inlA* (*L. innocua* [*inlA*]), nor with a strain of *Lm* that is deficient for the *hlyA* virulence gene, encoding the pore-forming toxin (PFT) listeriolysin O (LLO) (*Lm* Δ*hlyA*), affected CIRPB-210 to -201 relative abundances. As *L. innocua* does not harbor the *hlyA* gene, these results strongly suggest that LLO is a key determinant of CIRBP isoform switch, which is consistent with the activity of LLO being well-known to activate cellular stress response pathways (Besic et al., 2020; Gonzalez et al., 2011; Pillich et al., 2012; Tattoli et al., 2013).

The pore-forming activity of LLO is sufficient to induce CIRBP isoform switch

We next sought to determinate whether the pore-forming activity of LLO was required and sufficient for the induction of CIRBP isoform switch. To this end, we incubated LoVo cells with 4.5 nM of purified WT or mutated versions of LLO for 1 h, before assessing the relative abundance

of CIRBP isoforms (Figure 3B). Two of the variants of LLO used are mutated in the conserved undecapeptide of cholesterol-dependent PFTs (C484A or W492A), resulting in a respective loss of 70% and over 99% their hemolytic activity; the third mutant (Y206A) also displays an over 90% loss of hemolytic activity (Ribet et al., 2010). Exposure to WT LLO induced a 2.5-fold increase in the CIRPB-210 to -201 ratio, and the LLO mutant retaining 30% of its hemolytic activity also induced a 2-fold isoform switch. By contrast, catalytically inactive LLO mutants had no effect on CIRBP transcripts, thus emphasizing that LLO was sufficient to stimulate CIRBP isoform switch, and that its pore-forming activity was mechanistically involved in this process.

Consistent with the decrease in CIRBP protein abundance that was detected after 10 h of infection (Figure 2D), a decrease was observed by immunoblotting on total protein extracts from cells treated with 4.5 nM of LLO for 1 h (Figure 3C). This suggests that LLO-driven CIRBP isoform switch in favor of an NMD-sensitive transcript dampens CIRBP expression upon treatment by purified LLO as during *Lm* infection.

The switch in CIRBP isoform can be induced by a broad array of pore-forming toxins

As mentioned above, LLO belongs to the extended family of PFTs; more specifically, it is a cholesterol-dependent cytolysin (CDC) that creates 30-nm pores in membranes, although it can also be inserted as arcs or incomplete rings (Christie et al., 2018). To clarify the properties of cell membrane permeation that were responsible for LLO-mediated switch in CIRBP isoforms, the ability of other purified PFTs to induce this switch was assessed. Similarly to LLO, streptolysin O (SLO) and perfringolysin O (PFO) are CDCs that create large pores, while aerolysin (ALY) does not bind cholesterol but GPI-anchored proteins and forms pores of smaller diameter (1.5-2 nm) (Dal Peraro and van der Goot, 2016; Gonzalez et al., 2011). Using identical incubation conditions as for LLO — except that pro-aerolysin was activated for 10 min with trypsin (Krause et al., 1998)—, the three PFTs induced a 2.2- to 2.6-fold increase in isoform ratio (Figures 3D and 3E). CIRBP isoform regulation can thus be driven by the perforation of membranes, independently on pore-size. This suggests that a CIRBP-regulating cellular stimulus could be induced by the transit of ions or small solutes across the plasma membrane.

Perturbations of cationic gradients across the plasma membrane phenocopies LLO-induced switch in CIRBP isoform abundance

By forming pores in the plasma membrane, LLO and other PFTs lead to potassium effluxes as well as calcium and sodium influxes, thus altering the gradients of cation concentrations that are

actively maintained across the plasma membrane in living cells (Hamon and Cossart, 2011; Vadia and Seveau, 2014). To test if LLO-dependent cation leakage was involved in CIRBP regulation, cells were incubated in conditions that inhibit passive ion fluxes by using a high-potassium medium, to prevent potassium efflux, a calcium-free medium, to prevent calcium influx or a high-potassium and calcium-free medium to prevent both fluxes. Sodium concentrations were adjusted so that each medium remained isotonic, in order to avoid osmotic shock. Cells were accommodated for 30 min in each medium prior to LLO addition for 1 h, then CIRBP isoform ratio was assessed by RT-qPCR (Figure 3F). While cells incubated in the calcium-depleted medium behaved like cells in standard medium, with a 2-fold increase in the CIRBP-210 to -201 ratio in presence of LLO, a high extracellular potassium concentration alone was sufficient to induce a stronger switch CIRBP of CIRBP isoforms than LLO, whether in presence or absence of LLO or in calcium-depleted medium. Conversely, totally eliminating potassium from the extracellular medium led to a decrease in CIRBP-210/CIRBP-201 ratio that was not compensated by incubation with LLO (Figure 3G), suggesting that the balance between sodium and potassium concentrations across the plasma membrane has a strong influence on CIRBP regulation. Since LLO provokes potassium effluxes through membrane pores, one possible hypothesis for the nature of the signal that triggers CIRBP isoform switch would be a sensing of extracellular potassium concentration increase (and/or sodium decrease), or a cytotoxic effect of this ionic imbalance. An alternative —although intimately related— hypothesis would be that CIRBP isoform switch is triggered by perturbations of the plasma membrane potential as a result of cationic imbalance across the plasma membrane.

CIRBP alternative splicing is under control of CLK1 kinase activity in LoVo cells

A similar switch in CIRBP alternatively-spliced isoforms as the one we observed in response to *Lm* infection and to the activity of PFTs has already been reported to occur as a consequence of heat stress (Haltenhof et al., 2020; Neumann et al., 2020). This regulation has been directly linked to a loss of activity of the CLK1 kinase (Haltenhof et al., 2020). Upon heat stress, CLK1 inhibition was shown to shift the splicing of CIRBP in favor of CIRBP-210-like isoforms, likely through the dephosphorylation of serine/arginine-rich splicing factors, known as SR proteins, that are targets of CLK1 kinase activity (Haltenhof et al., 2020; Neumann et al., 2020). Consistently, treatment of LoVo cells with increasing concentrations of the CLK1 pharmacological inhibitor TG003 for 48 h shifted the splicing of CIRBP pre-mRNAs in favor of CIRBP-210 in a dose-response manner (Figure 4A), thus validating that CLK1 is a regulator of CIRBP isoform switch in LoVo cells, similar to what has been described in the HEK293 cell line (Haltenhof et al., 2020).

The processing of CLK1 pre-mRNA is altered upon infection

The expression of CLK1 itself is highly sensitive to heat stress (Ninomiya et al., 2011). Indeed, CLK1 mRNA is represented by two major forms: a mature protein-coding mRNA, and a premature, nuclear form in which introns 3 and 4 are retained (Retained Introns, RI). Upon heat stress, the dephosphorylation of CLK1 prevents its kinase activity on SR splicing factors (Haltenhof et al., 2020; Ninomiya et al., 2011). The subsequent dephosphorylation of SR proteins promotes the splicing of the IR pool into mature CLK1 mRNAs, which facilitates the rapid re-phosphorylation of SR splicing factors upon stress release (Ninomiya et al., 2011). To assess the effect of LLO-induced stress on CLK1 maturation, a region spanning exons 2 to 9 was amplified by PCR from cDNA prepared from cells that had been exposed to LLO for 15, 30, 45, or 60 min, or to 75 μM of TG003 for 1 h (Figure 4B). The pore-forming toxin stimulated the processing of CLK1 pre-mRNA from the IR form (top band) into its mature form (bottom band), with an intermediate form where the splicing between exons 3 and 4 was restored appearing after 15 min of treatment. The fully-spliced transcript accumulated after 45 min, until being nearly fully-spliced after 1 h of treatment, similarly to what is observed upon 1h of TG003-mediated CLK1 inhibition. LLO treatment can thus recapitulate the auto-regulatory processing of CLK1 transcripts that is a typical signature of CLK1 loss of activity and SR protein dephosphorylation, similar to what occurs upon heat stress (Ninomiya et al., 2011).

The phosphorylation and expression of SR splicing factors are impaired upon infection or LLO incubation

To determine the impact of *Lm*- or LLO-mediated regulation of CLK1 on its activity, the phosphorylation status of SR proteins was detected by specific immunoblotting against their phosphoepitopes at 1h post-treatment of cells with 4.5 nM of purified LLO. LLO induced a reduction of the phosphorylation level of SR proteins, best represented here by SRSF5 and SRSF6, by about 70% (Figures 4D and 4E).

The effects of SR proteins dephosphorylation on their activity is expected to affect the splicing of other genes than CIRBP, including SRSF genes that encode SR proteins themselves (Lareau et al., 2007; Müller-McNicoll et al., 2019; Risso et al., 2012). Consistently, nine SRSFs were affected by alternative splicing events at 10 hpi compared to NI cells (Figures 1A, S1A and S5). Among these, five (SRSF2, 3, 4, 6, and 7) were affected by shifts towards transcripts that harbor a “poison exon”, rendering them targets for degradation by NMD, and three (SRSF1, 5 and 10) resulted in noncoding alternative transcripts. Accordingly, the expression of these genes was dampened in infected cells, as attested by lower RNA levels and ribosome footprints (Figure S1B). These results corroborate a

model in which the stress generated during infection by the pore-forming activity of LLO leads to the dephosphorylation of SR-proteins *via* CLK1 inhibition, which in turns reshapes the cellular splicing
285 landscape, including by favoring the splicing of CIRBP pre-mRNAs towards NMD-sensitive isoforms, as well as that of SRSF pre-mRNAs towards unstable or noncoding transcripts.

CIRBP isoforms have opposite effects on cell infection

To investigate the possible consequences of CIRBP regulation as a player in the *Lm*-host crosstalk, isoform-specific knockdown was performed using siRNAs targeting either the CDS of CIRBP, which
290 targets both CIRBP-201 and -210 (siCIRBP-Total), the 3'-UTR of CIRBP-201 specifically (siCIRBP-201), or the 3'-UTR of CIRBP-210 specifically (siCIRBP-210) (Figure S6). After 48 h of RNA interference treatment, cells were infected with *Lm* for 10 h before enumerating intracellular bacteria (Figure 5A). Knocking down CIRBP-210 led to a 27% increase in colony forming units (cfu) per cell, while knocking down CIRBP-201 decreased the number of cfu/cell by 31%. Knock-down
295 of both RNA isoforms displayed an intermediate phenotype with a non-significant 14% decrease in infection. These results hint at a role for CIRBP in the control of cell autonomous response to infection, and emphasize the contribution of CIRBP isoform switch as a key event in opposing the colonization of cells by bacteria, by dampening the expression of a pro-bacterial protein-coding isoform in favor of a less stable transcript and of decreased protein expression.

300 **CIRBP mRNA targets shift from housekeeping- to stress response- related functions upon infection.**

As CIRBP acts as a regulator of gene expression by binding its target mRNAs, we compared the sets of CIRBP targets between non-infected and infected cells by RNA-immunoprecipitation of CIRBP followed by Illumina sequencing of co-precipitated mRNAs (RIP-seq) (Table S2). From a
305 total of 242 identified mRNA targets, a common core of 146 genes were similarly enriched in CIRPB immunoprecipitations (IPs) in both conditions (Figure 5B). By contrast, two distinct sets of gene transcripts were preferentially bound by CIRBP depending on infection; 28 targets were preferentially enriched in non-infected cells (Figure 5B, blue dots; Figure 5C), and 68 others were preferentially enriched in infected cells (Figure 5B, pink dots; Figure 5D), likely reflecting a reallocation of CIRBP
310 regulatory activity on cellular mRNAs in response to infection. Comparison of the sets of CIRPB-bound targets by gene ontology overrepresentation analysis highlighted an overall shift in the functions of their products between the two conditions (Figure S7). Enrichment for functions associated with transcription, organization of the cytoskeleton and metal cation binding were lost upon infection, in favor of functions associated with cellular response to stress, DNA replication and

315 repair, and regulation of metabolic processes. Altogether, the observed changes in the set of CIRBP targets suggest that infection-induced control of CIRBP activity contributes to the coordinated regulation orchestrating the cellular response to infection-induced stress.

Discussion

A broad range of damaging challenges trigger the activation of coordinated cell stress response
320 pathways that integrate signaling cascades and gene expression regulation. Among central players in the coordination of cell responses, CIRBP has previously be documented to regulate the expression of mRNAs involved in the modulation of the cell cycle and of inflammation, following exposure to multiple types of abiotic stressing agents (heat stress, UV or ionizing radiations, hypoxia, oxidative or osmotic stress, nutrient deprivation) or to viral infections (De Leeuw et al., 2007; Gokhale et al.,
325 2020; Zhong and Huang, 2017). Our findings extend the role of CIRBP to the control of cell autonomous resonses to biotic stress caused by bacterial PFTs upon a bacterial challenge, with downstream effects on the modulation of infection efficiency in a cell monolayer. In spite of the distinct nature of the initial stressors, our results highlight that the mechanisms of regulation of CIRBP by alternative splicing are shared between the previously-described response to heat stress
330 (Haltenhof et al., 2020; Neumann et al., 2020) and to PFT-dependent membrane damage. The exact nature of the unbalance that is sensed upon membrane permeation is currently unclear, as discriminating effects on intra/extracellular cation concentrations from that of a perturbation of the plasma membrane potential is a challenge.

Following stress sensing, the CLK1 kinase appears to play a key role as an integrator of distinct
335 types of damaging challenges by controlling the acvtivity of SR splicing factors, although the signalling pathways bridging stress sensing to the control of CLK1 activity are still elusive. CLK1-dependent inhibition of SR proteins reorients the splicing of specific cellular mRNAs, including CIRBP and CLK1 itself, towards the production of alternatively processed transcripts (Haltenhof et al., 2020; Ninomiya et al., 2011). Pre-mRNA processing of CIRBP is then shifted from the use of a
340 canonical 3'-UTR to an alternative 3'-UTR that contains a spliced intron. Upon splicing, deposition in the 3'-UTR of an exon junction complex that cannot be removed by translating ribosomes render this type of transcripts sensitive to NMD, and thus unstable (Le Hir et al., 2016). The stress-induced alternative splicing of CIRBP transcripts in favor of an NMD-sensitive RNA isoform thus lowers CIRBP expression in response to stress, which we have confirmed in the context of PFT-mediated
345 damage during bacterial infection.

In addition to quantitative effects on CIRBP mRNA stability due to NMD, the isoform switch in CIRBP that is observed upon *Lm* infection also impacts the sequence of the encoded protein products. Discriminating the impact of this protein sequence change from quantitative effects has not been addressed in the present study, nor in the existing literature, to the best of our knowledge, and is worthy of detailed investigation in the future. The divergence between CIRBP-201- and -210-encoded proteins only affects the last four AAs in the sequence, but entails the loss of a putative phosphorylation site previously hypothesized to participate in the nucleocytoplasmic partitioning if CIRBP (Yang et al., 2010), which is functionally important since the stress-induced translocation of CIRBP to the cytoplasm impacts it ability to bind and regulate its target genes (De Leeuw et al., 2007). Hence, a change in the localization or functionality of the CIRBP-210 product could take a share in the differential effect of the two isoforms on infection, rather than a purely quantitative effect due to altered RNA stability.

Our observation that expression of CIRBP-201 is rather pro-bacterial is consistent with a previous report where both the dominant CIRBP-201 and the low abundance -225-like protein-coding isoforms were found to have proviral effects, independently of their respective localizations (predominantly nuclear for the former, cytoplasmic for the latter) (Gokhale et al., 2020). Both findings hint at a detrimental effect of the main protein encoded by CIRBP in non-infected cells in the ability of epithelial cells to face infectious challenges. However, isoform-based regulation differs between the two studies. During viral infections, quantities of short-size CIRBP-201 (or -210, although it was not addressed in this study) products (CIRPB-S) remained stable, while levels of long-sized CIRBP-225 products (CIRBP-225) were reduced. By contrast, upon *Lm* infection we observed a reduction of CIRBP-201 levels and of CIRBP-S protein levels, while expression of CIRBP-225 —that we only assessed at the RNA level— was increased by 2.5-fold (Table S1G). Given these differences in expression, addressing the differential contribution of subdominant CIRBP-210 and -225 isoforms to the control of viral and bacterial infections, respectively, would deserve closer attention in the future.

Beyond their roles in human cells, roles for CIRBP homologs have been previously described in the adaptation of a broad range of multicellular eukaryotes to various types of environmental changes. In reptiles, the role of CIRBP has been reported to be involved in temperature-dependent sex-determination, in line with its role during moderate cold- or heat-exposure in mammals (Haltenhof et al., 2020; Schroeder et al., 2016). In plants, CIRBP homologs of the glycin-rich RNA-binding protein (GRP) family are involved in the control of innate immune responses to bacterial invaders as well as in cold adaptation and resistance to high salinity or drought (Kim et al., 2008, 2010; Nicaise et al., 2013). These similarities of involvement in the coordination of responses to biotic and abiotic stresses

across distant kingdoms of the Eukaryota hints at an ancient, conserved function of this family of proteins as key players in the coordination of defenses against pathogens and damaging environmental challenges.

Material and methods

Cellular model

LoVo cells, an intestinal epithelial cell line originating from a colon adenocarcinoma (male, ATCC CCL-229) were used as a model. Cells were maintained in DMEM, low glucose, GlutaMAX supplement, pyruvate medium (ThermoFisher Scientific, cat#21885025), supplemented with 10% heat-inactivated fetal bovine serum (PANBiotech, cat#p30-3306) in a humidified incubator at 37°C and 5% CO_2.

Bacterial strains

The bacterial source strains used for this work (Table S3) were *Listeria monocytogenes* LL195 as a main infection model and *Escherichia coli* NEB5α (New England BioLabs) for protein purification. *Listeria innocua* [*inlA*] and *L. monocytogenes* LL195 Δ*hlyA* were used for comparative purposes in infection assays. *E. coli* Top10(DE3) [pET29b-LLO-6His], *E. coli* Top10 [pET29b-LLO$_{C484A}$-6His], *E. coli* Top10 [pET29b-LLO$_{W492A}$-6His], *E. coli* Top10 [pET29b-LLO$_{Y206A}$-6His], *E. coli* DH5α [pTrcHisA-PFO], *E. coli* DH5α [pTrcHisA-SLO] and *E. coli* NEB5α [pET22b-PA-6His] were used as sources for the purification of pore-forming toxins. All strains were grown at 37°C under shaking at 180 rpm in Luria Bertani (LB) medium for *E. coli*, or in brain heart infusion (BHI) for *Lm* and *L. innocua* strains. Whenever required, media were supplemented with antibiotics for plasmid selection (chloramphenicol, 7μg/μL for *Lm* harboring a pAD vector and *inlA*-expressing *L. innocua*; kanamycin, 30 μg/μL for *E. coli* Top10 harboring pET29b vectors; and ampicillin, 100 μg/μL for *E. coli* DH5α and *E. coli* NEB5α harboring pTrcHisA and pET22b vectors).

Culture, transfection and infection of epithelial cells

Infections were performed in LoVo cells. Cells were between passage 7 and passage 15 before seeding and were grown to 80–85% confluence for 48 h prior to infection. When needed, cells were transfected 48 h before infection with 6 pg siRNAs against CIRBP-ORF, CIRBP-201 and CIRBP-210, UPF1 or scrambled siRNAs (Table S4A) using RNAiMAX in 12-well format as per manufacturer's recommendations (reverse transfection procedure). The decreases abundance of the corresponding proteins was confirmed by RT-qPCR and western blot.

One colony of bacteria was grown for about 16 h until they reached stationary phase (OD_{600} of 2 to 3) in 5 mL of BHI medium at 37°C. Bacteria were washed twice with PBS and added to the cell monolayer in culture flasks (for RNA-seq or RIP) or in 12-well plate format at the appropriate MOI (see Table S3A for details), by diluting bacteria to the appropriate density in serum-free DMEM. The cell culture flasks or plates were centrifuged at 200 × g for 1 min and then incubated at 37°C and 5% CO_2 for 1 h. Cells were then washed with PBS containing 25 μg/mL gentamicin, after which fresh medium containing 25 μg/mL gentamicin and 10% FBS was added. Infection was allowed to proceed until specific timepoints (2, 5 or 10 hpi, or uninfected for time 0), then culture plates were snap-frozen in liquid nitrogen and stored at −80°C until further use (for RNA or protein extraction or for RNA Immunoprecipitation (RIP)). Alternatively, for infection quantification, cells were washed in PBS and trypsinized for counting using a LUNA II automated cell counter, then centrifuged at 700 x g for 5 min. Cell pellets were resuspended in 500 μL ice-cold water and lysed by passing several times through a 26G needle. Cells lysates were diluted in water and plated on BHI before overnight incubation at 37°C. Colony-forming units (CFU) were counted and normalized to cell counts.

Immunoblot assays

Total cell lysate was prepared by adding RIPA (20 mM Tris-HCl pH 7.5, 150 mM NaCl, 1 mM EDTA, 1 mM EGTA, 1% IGEPAL, 1% Sodium Deoxycholate, 50 μg/μL PMSF) supplemented with protease inhibitor cocktail (Bimake, cat#B14011) and when needed, phosphatase inhibitor cocktail (Sigma, cat#P5726) directly to the cell monolayer. After scrapping of the monolayer, the lysate was transferred to an Eppendorf tube, incubated on ice for 10 min with intermittent vortex mixing, and then centrifuged for 10 min at 4°C at maximum speed. The supernatant was transferred to a fresh Eppendorf tube and the protein concentration was assessed using Bradford reagent (Abcam, cat#ab119216) and stored at -80°C when not used immediately. 40 μg of proteins were diluted in Laemmli sample buffer (SB 1X), after which samples were heated 95°C for 5 min and either stored at −80°C or used directly. Samples were separated by SDS-PAGE on a 12%-acrylamide gel and transferred to Amersham Protran 0.2 μM nitrocellulose membranes using a Mini Trans-Blot cell (Bio-Rad) for 1 h at 100 V at 4°C in chilled transfer buffer (Tris-Base 3 g/L, Glycine 1.4 g/L, 20% ethanol). Membranes were blocked for 30 min in PBS or TBS containing 0.1% of Tween 20 (PBS-T and TBS-T, respectibely) and 5% milk or bovine serum albumin (BSA), according to antibody manufacturer's recommendations. Primary antibodies were added to the blocking solutions at the recommended dilution before overnight incubation at 4°C. Anti-CIRBP (Proteintech, cat#10209-2-AP, 1:500 dilution); anti-β-Tubulin (Biolegend, cat#903401, 1:2,000 dilution); anti-GAPDH (Cell Signaling Technologies, cat#2118, 1/1,000 dilution); anti-SR proteins (Millipore, cat#MABE126,

1:2,000 dilution); anti-phosphoepitope SR proteins clone1H4 (Millipore, cat#MABE50, 1:2,000 dilution) were used as primary antibodies. Membranes were washed three times in PBS-T or TBS-T and incubated with the corresponding secondary antibody (Bethyl anti mouse or rabbit IgGs coupled to HRP, cat#A120101P and A90-116P, respectively) at a 1:50,000 dilution in the same buffer for 2 h at room temperature. Signals were revealed using Pierce ECL or ECL Plus Western Blotting Substrates (ThermoFisher Scientific, cat#32106 and #32132, respectively) on an Las4000 imager (Amersham).

RNA extraction and RT-qPCR

From a 12-wells plate format, total RNA was extracted by adding 300 μL of TriReagent (MRC, cat#TR118) directly onto the cell monolayer and following the extraction procedure according to the manufacturer's instructions. After ethanol precipitation, RNA was resuspended in 44 μL of RNase-free water, to which 5 μL of Turbo DNase 10X Buffer and 1μL of Turbo DNAse (Thermo Scientific, cat#AM2238) were added, before a 30-min incubation at 37°C to eliminate genomic DNA. RNA was again purified by extraction with acid phenol:chloroform (Invitrogen, cat#AM9722) followed by precipitation with ethanol according to the manufacturer's instructions, and then stored at -80°C or used immediately. 500 ng of RNA were used for reverse transcription with the SuperScript IV First-Strand Synthesis Kit (Invitrogen, cat#18091200) using random hexamers, according to the manufacturer's instructions. RNA was degraded with 1 μL of RNase A (Thermo Scientific, cat# R1253) for 30 min at 37°C. The final product was diluted to 1:20 and 2 μL of the dilution were used in each 10-μl RT-qPCR reaction along with 400 nM of primers gene- or isoform-specific primers (Table S4B) and 1X SensiFAST SYBR No-ROX Mix (Bioline, cat#BIO-98005). Quantitative PCR was performed in CFX384 Touch Real-Time PCR Detection System (Biorad). Each reaction was performed in triplicate. Normalized relative gene expression was determined using the mean Cq of each technical triplicate, and following the $2^{-\Delta\Delta Cq}$ method with *GAPDH* as a reference gene.

Purification of recombinant pore-forming toxins

PFT-expressing plasmids were purified from an overnight stationary culture of the corresponding strain by using the Wizard Plus SV Minipreps DNA purification System (Promega, cat#A1460) and transformed into *E. coli* BL21 (DE3) (New England Biolabs, cat#C2527H). Positive clones were screened by colony PCR, 3-4 positive colonies were inoculated in 20 mL of LB containing the appropriate antibiotic and incubated at 37°C, 180 rpm for 6 h to reach stationary phase. This starter culture was used to inoculate 1L of LB containing antibiotics. Incubation was pursued under shaking until a OD_{600nm} of 0.8 was reached. Isopropyl β-D-1-thiogalactopyranoside (IPTG) was then added at

a final concentration of 0.5 mM and the culture was incubated overnight at 16°C. Bacteria were
475 collected by centrifugation at 3,600 × g for 10 min at 4°C. The pellet was washed once with ice-cold PBS and resuspended in lysis buffer (1.5 X PBS, 1 mM magnesium acetate, 0.1% IGEPAL, 20 mM leupeptin, 1 μg/mL pepstatin, 50 μg/mL PMSF and 1 X Lysozyme), sonicated for 4 min and centrifuged for 30 min at 27,000 x g, 4°C. The supernatant was collected in a fresh 50 mL tube, mixed with 250 μL of Ni-NTA agarose resin (Invitrogen, cat#R901-15), that had been preequilibrated in an
480 equal volume of lysis buffer, and the slurry was incubated for 2 h on a rotating device at 4°C. The resin was pelleted by centrifugation at 500 x g for 15 min, 4°C, washed twice with 5 mL of lysis buffer, then once with 500 μL of wash buffer (1.5X PBS, 250 mM NaCl, 1 mM magnesium acetate, 0.1% Igepal CA-630, 50 mM imidazole, 10% glycerol) and once more with 5 ml of lysis buffer. The beads, resuspended in 1 mL if lysis buffer, were transferred to a Poly-Prep Chromatography column
485 (Biorad, cat# 731-1550) and the remaining supernatant was let to flow through. The slurry was incubated for 5 min on the column with 800 μL of elution buffer (1.5 X PBS, 1 mM magnesium acetate, 0.1% Igepal CA-3, 150 mM imidazole, 10% glycerol), then the eluate was collected, before proceeding to elution of another fraction (10 times). The concentration of each fraction was determined with Bradford Reagent (Abcam, cat#ab119216) and fractions with an absorbance above
490 0.1 were pooled and dialyzed overnight in 1L dialysis buffer (1.5X PBS, 1mM magnesium acetate, 10% glycerol and 2 mM dithiothreitol (DTT)) in 12-14 kDa Spectra/Por dialysis tubing (Repligen, cat#123697) with mild agitation at 4°C. The dialyzed protein solution was diluted in protein storage solution (20 mM MES pH 5.7, 150 mM NaCl, 5% glycerol, 2 mM DTT), aliquoted at 0.1 μM and stored at -80°C. Protein purity was assessed by running samples of every step of the purification
495 process on SDS-PAGE and staining the gel using Quick Coomassie Stain (Neo-Biotech, cat#NB-45-00078) to reveal single bands in the eluted and dialyzed fractions.

Before use, pro-aerolysin was activated by incubation for 10 min with trypsin in a 1:20 aerolysin:trypsin molar ratio, then trypsin was inactivated by adding trypsin inhibitor (PromoCell cat#C-41120) to a final concentration of 0.02%.

500 **Treatment of cells with pore-forming toxins or with pharmacological inhibitors**

LoVo cells were seeded in 12-wells plates at an appropriate to reach 85-90% confluence 48 h later. For TG003 treatment and PFTs treatment, the cells were washed once with PBS, then serum-free medium supplemented with PFTs at 4.5 nM, or with TG003 at a concentration ranging from 10 to 100 μM was added for 1h. Because aerolysin had been activated with trypsin, a similar
505 concentration of inactivated trypsin diluted in the same buffer was added in the control sample. Cells

were washed once with cold PBS, snap-frozen in liquid nitrogen and stored at −80°C until further use.

Ion fluxes perturbation

To test the role of calcium and potassium, isotonic calcium-free and high-potassium media were prepared according to Vadia & Seveau, 2014. Potassium-free medium was prepared similarly to the Standard medium but lacked KCl. High-potassium$^+$/calcium-free medium was prepared similarly to the high-potassium medium but lacked $CaCl_2$. LoVo cells were seeded 48 h prior to experiment in a 12-wells plate format to reach 85-90% confluency. Cells were washed once with PBS and incubated for 30 min in the corresponding ion-altered medium prior to LLO 4.5 nM addition or not. Cells were incubated for another hour, then washed once with cold PBS, snap-frozen in liquid nitrogen and stored at −80°C until further use.

Immunofluorescence staining, epifluorescence microscopy and image analysis

LoVo cells were seeded in 24-well plates containing 12-mm diameter coverslips. Infection with *Lm* was performed as described above. At 10 hpi, cells were fixed for 15 min with 4% paraformaldehyde in PBS, washed with PBS then stored at 4°C until further processing. Prior to immunofluorescence staining, cells were permeabilized for 5 min at 20°C with 0.5% Triton X-100 in PBS. Cells were then blocked for 30 min in PBS buffer containing 2% BSA, then incubated with a 1:500 dilution of anti-CIRBP antibody (Proteintech, cat#10209-2-AP) in the same buffer. After three washes in PBS, samples were incubated with Cy3-goat-anti-rabbit secondary antibody (Jackson ImmuneResearch cat#111-165-144, 1:500 dilution), Acti-stain 488 phalloidin (Cytoskeleton #PHDG1-A, 70 nM) and 4',6-diamidino-2-phenylindole (DAPI, 100 ng/ml) in PBS for 1 h. After three additional washes, coverslips were mounted on microscope slides with Fluoromount mounting medium (Interchim).

Preparations were observed with a Nikon Ti epifluorescence microscope (Nikon), connected to a digital CMOS camera (Orca Flash 4.0, Hamamatsu). Illumination was achieved using a SOLA-SE 365 source (Lumencor) and the following excitation/emission/dichroic filter sets (Semrock): DAPI, 377(50)/447(60)/FF409-Di03; Acti-Stain 488, 472(30)/520(35)/FF495-Di03; and Cy3, 543(22)/586(20)/4FF562-TRITC. Images were acquired with Nikon apochromat 60X objective lenses (NA 1.4) and processed with the MicroManager and Fiji software. Each image is representative of the infected cell population.

Long-read RNA-seq sample and library preparation

The RNA samples used from long-read cDNA sequencing (long-read RNA-seq) were the same ones that had been prepared in our previous work for total cytoplasmic RNA sequencing with Illumina next-generation sequencing technology (short-read RNA-seq) of *Lm*-infected LoVo cells over a 10-h time course (Besic et al., 2020). Briefly, LoVo cells had been grown in 75 cm^2 flasks, infected with *Lm* LL195 and snap-frozen as described above. Lysis buffer (20 mM Tris pH 7.4, 150 mM NaCl, 5 mM MgCl2, 1% Triton X-100, 1 mM DTT, 25 U/ml DNase TURBO, Invitrogen cat#AM2238) had been added to the frozen monolayer, which had then been scrapped and transferred to an Eppendorf tube and processed as described above for RNA extraction. Each of the sample sets was reproduced at 1-week interval. The integrity of isolated RNA was verified using the RNA Pico kit on an Agilent 2100 Bioanalyzer. Only high-quality RNA (RIN > 8) was used in library preparation.

Library preparation was performed using SQK-LSK108 following manufacturer's protocol (1D PCR Barcoding cDNA; ONT) optimized for cDNA sequencing. Briefly, 100 ng of total RNA was reverse-transcribed for each sample with SuperScript IV (Life Technologies, cat#18090010), using custom polyT-VN and strand switching primers at 50°C for 10 min. Template switching was pertformed at 42°C for 10 min and enzyme inactivation at 80°C for 10 min. The reaction was purified with 0.7X Agencourt Ampure XP beads. A quarter of the purified RT product was taken into PCR for amplification and barcodes addition (Barcoded primers form EXP-PBC001, ONT), with a 17-min elongation at each 18 cycles. Double stranded cDNA was purified as above, quantified and checked for the size. Sample were multiplexed in equimolar quantities to obtain 1 μg of cDNA. The pool was end-repaired and dA-Tailed using the NEBNext End repair / dA-tailing Module (New England BioLabs, cat#E7546), and purified with 1X Agencourt beads. Adapter ligation was performed at 20°C for 10 min, with Adapter Mix (AMX, ONT) and Blunt/TA Ligase Master Mix (New England BioLabs, cat# M0367). After a final 1X clean-up and washing of the beads with Adapter Binding Buffer (ABB, ONT), the library was eluted in 15 μL Elution buffer. 900 ng of cDNA was loaded on an R9.4.1 flowcell after priming it according to the manufacturer's protocol. Sequencing was performed with the standard 48-hour sequencing protocol run on the MinION MkIB, using the MinKNOW software (versions 1.7.1, 1.7.4, and 1.10.23). A mean of 1,7 ± 0,5million passing ONT quality filter reads was obtained for each of the 12 samples. Base-calling from read event data was performed by guppy-3.6.1.

RNA Immunoprecipitation sample and sequencing library preparation (RIP-seq)

LoVo cells were cultured in 75 cm^2 flasks and infected as described above. RIP was performed according to Kwon et al. until RNA resuspension (Kwon et al., 2021), except only IP 150 buffer was used for beads washing, and the antibodies used were anti-CIRBP or control IgG from rabbit serum (Sigma, cat#I5006). Two flasks per condition were pooled during final precipitation. Purified input or RIP-seq RNA samples were resuspended in 15 μL of water, their concentration was assessed by Qubit RNA High Sensitivity kit (Invitrogen, cat#Q32852) and samples were stored at -80°C until further processing.

For library preparation and Illumina sequencing, messenger (polyA$^+$) RNAs were purified from 25 ng of RIP samples and 500 ng of total RNA input using oligo(dT). Libraries were prepared using the strand specific RNA-seq library preparation Stranded mRNA ligation kit (Illumina). Libraries were multiplexed by 12 for RIP samples and by 6 for input samples on P2 flowcell. A 118-bp single read sequencing was performed on a NextSeq 2000 (Illumina). A mean of 41 ± 19 million reads passing Illumina quality filter reads for RIP samples, and 88 ± 10 million reads for input samples, was obtained.

Read processing for long-read RNA-seq and RIP-seq

Long-read and RIP-Seq data discussed in this publication will be deposited in the ArrayExpress database (https://www.ebi.ac.uk/biostudies/arrayexpress) and released upon publication. Fastq files quality was checked on Galaxy servers using the FastQC tool. Reads mapping to the 5S ribosomal RNA (OX177011.1) or 45S (NR_046235.3) pre-ribosomal RNA sequences with Bowtie2 (Galaxy Version 2.5.0) were filtered out. For long-read RNA-seq, filtered reads were mapped to the human genome (Grch38.p13 from Gencode) using minimap2 (Galaxy Version 2.24) with enabled spliced alignments. For RIP-Seq, filtered reads were mapped to Grch38.p13 using RNA-STAR (Galaxy Version 2.7.8a) and a gene model file for splice junction (gencode.v41.annotation.gff3). Read processing for short-read RNA-seq data was described previously (Besic et al., 2020).

Alternative splicing analysis

Alternative splicing analysis was performed following the MAJIQ algorithm tutorial. Alignment files for short-read RNA-seq were used along with the latest Gencode annotation file (gencode.v41.annotation.gff3) as inputs for the MAJIQ builder step. The deltaPSI method was used to run the MAJIQ quantifier, and results were modulized in VOILA (--changing-between-group-dpsi 0.05 --decomplexify-psi-threshold 0.01). Final results were visualized in the VOILA application as

instructed. AS events were considered biologically relevant for |ΔPSI| between 10 hpi and non-infected cells over 0.1, and a probability of changing over 0.95. Functional enrichment analysis for genes significantly impacted by an AS event was conducted using over-representation analysis of GO biological processes with the gprofiler2 R package (version 0.2.1).

Long reads data analysis

Long-reas RNA-seq alignment files were directly used to discover and quantify transcript isoforms by using the Bambu package in R (Chen et al., 2022, version 2.2.0) and the latest Gencode annotation file (gencode.v41.annotation.gff3), generating a table of normalized transcript counts. From these tables, differential usage of the transcript isoforms was quantified with the IsoformSwitchAnalyzeR package in R (Vitting-Seerup and Sandelin, 2019, version 1.18.0). Information on impacted transcripts IDs and types were extracted from the Ensembl database (https://www.ensembl.org) using BioMart (version 2.52.0). Uniquely mapped reads were counted using FeatureCounts (version 2.0.1). Library size-normalized read alignments were visualized using the Integrative Genomics Viewer (IGV) from bedGraph files generated using samtools and bedtools.

RIP-Seq data analysis

Differential target enrichment of RIP-seq data were quantified by identifying enriched genes in CIRBP IP fractions compared (1) to the corresponding input fractions, and (2) to the corresponding control IgG IP fractions in two parallel analyses, using DESeq2 in R (version 1.36). CIRBP targets were considered as significantly enriched if they matched criteria of p_{adj} <0.05 and $\log_2$FC > 0.5 in both comparisons. For volcano plots, gene enrichment repartition for both non-infected and *Lm*-infected conditions was represented using values from the IP versus control IgG DESeq2 analysis. Functional enrichment analysis for significant CIRBP targets was conducted using over-representation analysis of GO biological processes with the gprofiler2 R package version 0.2.1.

Acknowledgements

We are grateful to Dominique Weil, Lionel Navarro, Laetitia Vincensini, Hervé Le Hir, Isabelle Barbosa, Lucia Morillo, Nadia Ruiz-Gutierrez, Brice Sperandio, Caroline Peron-Cane, Thomas Petit and Simon Guette-Marquet for precious scientific discussion, methodological advice and kind help, and to Olivier Disson for reagents sharing. Research in AL's group received support from Mairie de Paris (programme Émergence(s) Recherche médicale) and under the program "Investissements d'Avenir" managed by the French national research agency (ANR-10-LABX-54 MemoLife and

ANR-10-IDEX-0001-02 PSL). The GenomiqueENS core facility was supported by the France Génomique national infrastructure, funded as part of the "Investissements d'Avenir" program managed by the French national research agency (ANR-10-INBS-09).

Author contributions

AL initiated and supervised the study. MC and AL devised the research hypotheses and methodology, and interpreted results. MC performed most experiments. VBe provided RNA samples for long-read RNA-seq and methodological advice. CSB prepared sequencing libraries and performed sequencing at the École normale superieure genomics core facility. AK and AV performed CIRBP localization studies under supervision by MC. MC analysed sequencing data with advice and input from VBoe, LJ and MTC. MC and AL wrote the manuscript.

Declaration of interests

The authors declare no competing interests. Funders had no role in the orientation of research.

References

1. Al-Fageeh, M.B., Smales, C.M., 2009. Cold-inducible RNA binding protein (CIRP) expression is modulated by alternative mRNAs. RNA 15, 1164–1176.
2. Besic, V., Habibolahi, F., Noël, B., Rupp, S., Genovesio, A., Lebreton, A., 2020. Coordination of transcriptional and translational regulations in human epithelial cells infected by *Listeria monocytogenes*. RNA Biol. 17, 1492–1507.
3. Boehm, V., Kueckelmann, S., Gerbracht, J.V., Kallabis, S., Britto-Borges, T., Altmüller, J., Krüger, M., Dieterich, C., Gehring, N.H., 2021. SMG5-SMG7 authorize nonsense-mediated mRNA decay by enabling SMG6 endonucleolytic activity. Nat. Commun. 12, 3965.
4. Celli, J., Tsolis, R.M., 2015. Bacteria, the endoplasmic reticulum and the unfolded protein response: friends or foes? Nat. Rev. Microbiol. 13, 71–82.
5. Chen, Y., Sim, A., Wan, Y.K., Yeo, K., Lee, J.J.X., Ling, M.H., Love, M.I., Göke, J., 2022. Context-aware transcript quantification from long read RNA-seq data with Bambu. BiorRxiv.
6. Christie, M.P., Johnstone, B.A., Tweten, R.K., Parker, M.W., Morton, C.J., 2018. Cholesterol-dependent cytolysins: from water-soluble state to membrane pore. Biophys. Rev. 10, 1337–1348.
7. Dal Peraro, M., van der Goot, F.G., 2016. Pore-forming toxins: ancient, but never really out of fashion. Nat. Rev. Microbiol. 14, 77–92.

8. De Leeuw, F., Zhang, T., Wauquier, C., Huez, G., Kruys, V., Gueydan, C., 2007. The cold-inducible RNA-binding protein migrates from the nucleus to cytoplasmic stress granules by a methylation-dependent mechanism and acts as a translational repressor. Exp. Cell Res. 313, 4130–4144.
9. Eldridge, M.J.G., Cossart, P., Hamon, M.A., 2020. Pathogenic biohacking: Induction, modulation and subversion of host transcriptional responses by *Listeria monocytogenes*. Toxins 12, 294.
10. Farrand, A.J., LaChapelle, S., Hotze, E.M., Johnson, A.E., Tweten, R.K., 2010. Only two amino acids are essential for cytolytic toxin recognition of cholesterol at the membrane surface. Proc. Natl. Acad. Sci. U. S. A. 107, 4341–4346.
11. Fulda, S., Gorman, A.M., Hori, O., Samali, A., 2010. Cellular stress responses: Cell survival and cell death. Int. J. Cell Biol. 2010, 214074.
12. Galluzzi, L., Yamazaki, T., Kroemer, G., 2018. Linking cellular stress responses to systemic homeostasis. Nat. Rev. Mol. Cell Biol. 19, 731–745.
13. Glomski, I.J., Gedde, M.M., Tsang, A.W., Swanson, J.A., Portnoy, D.A., 2002. The *Listeria monocytogenes* hemolysin has an acidic pH optimum to compartmentalize activity and prevent damage to infected host cells. J. Cell Biol. 156, 1029–1038.
14. Gokhale, N.S., McIntyre, A.B.R., Mattocks, M.D., Holley, C.L., Lazear, H.M., Mason, C.E., Horner, S.M., 2020. Altered m6A modification of specific cellular transcripts affects flaviviridae infection. Mol. Cell 77, 542-555.e8.
15. Gonzalez, M.R., Bischofberger, M., Frêche, B., Ho, S., Parton, R.G., van der Goot, F.G., 2011. Pore-forming toxins induce multiple cellular responses promoting survival. Cell. Microbiol. 13, 1026–1043.
16. Haltenhof, T., Kotte, A., Bortoli, F.D., Schiefer, S., Meinke, S., Emmerichs, A.-K., Petermann, K.K., Timmermann, B., Imhof, P., Franz, A., Loll, B., Wahl, M.C., Preußner, M., Heyd, F., 2020. A conserved kinase-based body-temperature sensor globally controls alternative splicing and gene expression. Mol. Cell 78, 57-69.e4.
17. Hamon, M.A., Cossart, P., 2011. K^+ efflux Is required for histone H3 dephosphorylation by *Listeria monocytogenes* listeriolysin O and other pore-forming toxins. Infect. Immun. 79, 2839–2846.
18. Horii, Y., Shimaoka, H., Horii, K., Shiina, T., Shimizu, Y., 2019. Mild hypothermia causes a shift in the alternative splicing of cold-inducible RNA-binding protein transcripts in Syrian hamsters. Am. J. Physiol.-Regul. Integr. Comp. Physiol. 317, R240–R247.
19. Iacovache, I., Paumard, P., Scheib, H., Lesieur, C., Sakai, N., Matile, S., Parker, M.W., van der

Goot, F.G., 2006. A rivet model for channel formation by aerolysin-like pore-forming toxins. EMBO J. 25, 457–466.

20. Kammoun, H., Kim, M., Hafner, L., Gaillard, J., Disson, O., Lecuit, M., 2022. Listeriosis, a model infection to study host-pathogen interactions *in vivo*. Curr. Opin. Microbiol. 66, 11–20.
21. Kim, J.S., Jung, H.J., Lee, H.J., Kim, K.A., Goh, C.-H., Woo, Y., Oh, S.H., Han, Y.S., Kang, H., 2008. Glycine-rich RNA-binding protein 7 affects abiotic stress responses by regulating stomata opening and closing in *Arabidopsis thaliana*. Plant J. Cell Mol. Biol. 55, 455–466.
22. Kim, J.Y., Kim, W.Y., Kwak, K.J., Oh, S.H., Han, Y.S., Kang, H., 2010. Glycine-rich RNA-binding proteins are functionally conserved in *Arabidopsis thaliana* and *Oryza sativa* during cold adaptation process. J. Exp. Bot. 61, 2317–2325.
23. Knowles, A., Campbell, S., Cross, N., Stafford, P., 2021. Bacterial manipulation of the integrated stress response: A new perspective on infection. Front. Microbiol. 12.
24. Krause, K.-H., Fivaz, M., Monod, A., van der Goot, F.G., 1998. Aerolysin induces G-protein activation and Ca^{2+} release from intracellular stores in human granulocytes. J. Biol. Chem. 273, 18122–18129.
25. Kwon, O.S., Mishra, R., Safieddine, A., Coleno, E., Alasseur, Q., Faucourt, M., Barbosa, I., Bertrand, E., Spassky, N., Le Hir, H., 2021. Exon junction complex dependent mRNA localization is linked to centrosome organization during ciliogenesis. Nat. Commun. 12, 1351.
26. Lareau, L.F., Inada, M., Green, R.E., Wengrod, J.C., Brenner, S.E., 2007. Unproductive splicing of SR genes associated with highly conserved and ultraconserved DNA elements. Nature 446, 926–929.
27. Le Hir, H., Saulière, J., Wang, Z., 2016. The exon junction complex as a node of post-transcriptional networks. Nat. Rev. Mol. Cell Biol. 17, 41–54.
28. Lecuit, M., Ohayon, H., Braun, L., Mengaud, J., Cossart, P., 1997. Internalin of *Listeria monocytogenes* with an intact leucine-rich repeat region is sufficient to promote internalization. Infect. Immun. 65, 5309–5319.
29. Lujan, D.A., Ochoa, J.L., Hartley, R.S., 2018. Cold-inducible RNA binding protein in cancer and inflammation. WIREs RNA 9, e1462.
30. Müller-McNicoll, M., Rossbach, O., Hui, J., Medenbach, J., 2019. Auto-regulatory feedback by RNA-binding proteins. J. Mol. Cell Biol. 11, 930–939.
31. Neumann, A., Meinke, S., Goldammer, G., Strauch, M., Schubert, D., Timmermann, B., Heyd, F., Preußner, M., 2020. Alternative splicing coupled mRNA decay shapes the temperature-dependent transcriptome. EMBO Rep. 21, e51369.
32. Nicaise, V., Joe, A., Jeong, B., Korneli, C., Boutrot, F., Westedt, I., Staiger, D., Alfano, J.R.,

725 Zipfel, C., 2013. Pseudomonas HopU1 modulates plant immune receptor levels by blocking the interaction of their mRNAs with GRP7. EMBO J. 32, 701–712.

33. Ninomiya, K., Kataoka, N., Hagiwara, M., 2011. Stress-responsive maturation of Clk1/4 pre-mRNAs promotes phosphorylation of SR splicing factor. J. Cell Biol. 195, 27–40.
34. Ode, Y., Aziz, M., Jin, H., Arif, A., Nicastro, J.G., Wang, P., 2019. Cold-inducible RNA-binding
730 protein induces neutrophil extracellular traps in the lungs during sepsis. Sci. Rep. 9, 6252.
35. Pakos-Zebrucka, K., Koryga, I., Mnich, K., Ljujic, M., Samali, A., Gorman, A.M., 2016. The integrated stress response. EMBO Rep. 17, 1374–1395.
36. Pillich, H., Chakraborty, T., Mraheil, M.A., 2015. Cell-autonomous responses in *Listeria monocytogenes* infection. Future Microbiol. 10, 583–597.
735 37. Pillich, H., Loose, M., Zimmer, K.-P., Chakraborty, T., 2012. Activation of the unfolded protein response by *Listeria monocytogenes*. Cell. Microbiol. 14, 949–964.
38. Qiang, X., Yang, W.-L., Wu, R., Zhou, M., Jacob, A., Dong, W., Kuncewitch, M., Ji, Y., Yang, H., Wang, H., Fujita, J., Nicastro, J., Coppa, G.F., Tracey, K.J., Wang, P., 2013. Cold-inducible RNA-binding protein (CIRP) triggers inflammatory responses in hemorrhagic shock and sepsis.
740 Nat. Med. 19, 1489–1495.
39. Ribet, D., Hamon, M., Gouin, E., Nahori, M.-A., Impens, F., Neyret-Kahn, H., Gevaert, K., Vandekerckhove, J., Dejean, A., Cossart, P., 2010. *Listeria monocytogenes* impairs SUMOylation for efficient infection. Nature 464, 1192–1195.
40. Risso, G., Pelisch, F., Quaglino, A., Pozzi, B., Srebrow, A., 2012. Regulating the regulators:
745 serine/arginine-rich proteins under scrutiny. IUBMB Life 64, 809–816.
41. Rodrigues, L.O.C.P., Graça, R.S.F., Carneiro, L.A.M., 2018. Integrated stress responses to bacterial pathogenesis patterns. Front. Immunol. 9.
42. Schroeder, A.L., Metzger, K.J., Miller, A., Rhen, T., 2016. A novel candidate gene for temperature-dependent sex determination in the common snapping turtle. Genetics 203, 557–571.
750 43. Shrestha, N., Bahnan, W., Wiley, D.J., Barber, G., Fields, K.A., Schesser, K., 2012. Eukaryotic initiation factor 2 (eIF2) signaling regulates proinflammatory cytokine expression and bacterial invasion. J. Biol. Chem. 287, 28738–28744.
44. Tattoli, I., Sorbara, M.T., Yang, C., Tooze, S.A., Philpott, D.J., Girardin, S.E., 2013. *Listeria* phospholipases subvert host autophagic defenses by stalling pre-autophagosomal structures.
755 EMBO J. 32, 3066–3078.
45. Vadia, S., Seveau, S., 2014. Fluxes of Ca^{2+} and K^{+} are required for the listeriolysin O-dependent internalization pathway of *Listeria monocytogenes*. Infect. Immun. 82, 1084–1091.
46. Vaquero-Garcia, J., Barrera, A., Gazzara, M.R., González-Vallinas, J., Lahens, N.F., Hogenesch,

J.B., Lynch, K.W., Barash, Y., 2016. A new view of transcriptome complexity and regulation through the lens of local splicing variations. eLife 5, e11752.

47. Vitting-Seerup, K., Sandelin, A., 2019. IsoformSwitchAnalyzeR: analysis of changes in genome-wide patterns of alternative splicing and its functional consequences. Bioinformatics 35, 4469–4471.
48. Weinmaier, T., Riesing, M., Rattei, T., Bille, J., Arguedas-Villa, C., Stephan, R., Tasara, T., 2013. Complete genome sequence of *Listeria monocytogenes* LL195, a serotype 4b strain from the 1983-1987 listeriosis epidemic in Switzerland. Genome Announc. 1, e00152-12.
49. Xia, Z., Zheng, X., Zheng, H., Liu, X., Yang, Z., Wang, X., 2012. Cold-inducible RNA-binding protein (CIRP) regulates target mRNA stabilization in the mouse testis. FEBS Lett. 586, 3299–3308.
50. Yang, C., Carrier, F., 2001. The UV-inducible RNA-binding protein A18 (A18 hnRNP) plays a protective role in the genotoxic stress response. J. Biol. Chem. 276, 47277–47284.
51. Yang, R., Zhan, M., Nalabothula, N.R., Yang, Q., Indig, F.E., Carrier, F., 2010. Functional significance for a heterogenous ribonucleoprotein A18 signature RNA motif in the 3'-untranslated region of ataxia telangiectasia mutated and Rad3-related (ATR) transcript. J. Biol. Chem. 285, 8887–8893.
52. Zhong, P., Huang, H., 2017. Recent progress in the research of cold-inducible RNA-binding protein. Future Sci. OA 3, FSO246.

Figures

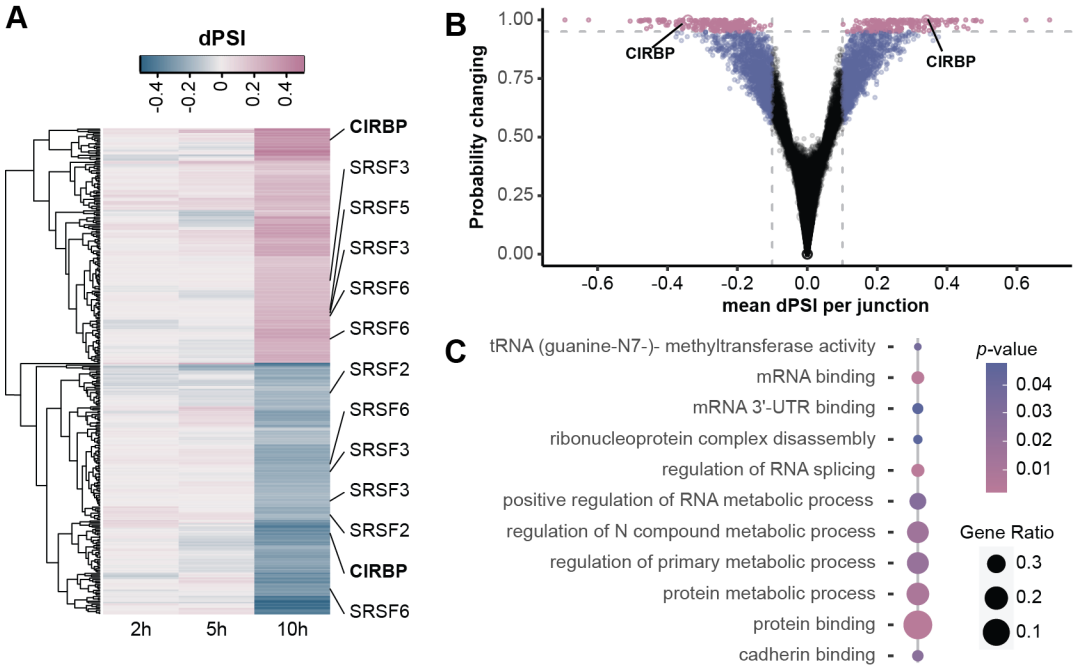

Figure 1. *Lm* infection alters the representation of mRNA isoforms for a subset of human genes, including CIRBP

(A-C) Variations in the abundance of mRNA isoforms in LoVo intestinal epithelial cells infected for 2 to 10 h. Total cytoplasmic RNAs were processed for long-read and short read cDNA sequencing. Data from three independent replicates.

(A) Heatmap of the difference at 2, 5 and 10 hpi in percentage spliced-in (dPSI) values of significant alternative splicing events induced by *Lm* infection, compared with non-infected cells (probability of changing > 0.95).

(B) Volcano plots highlighting the most significant alternative splicing events in *Lm*-infected cells at 10 hpi compared to non-infected cells. Data points represent alternative splicing (AS) events with a probability of changing over 95%. Vertical dashed grey lines indicate a mean dPSI of 0.1 and the horizontal dashed gray line indicates a probability of changing of 0.95.

(C) Over-representation analysis (ORA) of GO biological process terms for genes undergoing RNA isoform-based regulation in LoVo cells at 10 hpi compared to non-infected conditions (probability of changing > 0.95; all dPSI beyond this threshold were above 0.1).

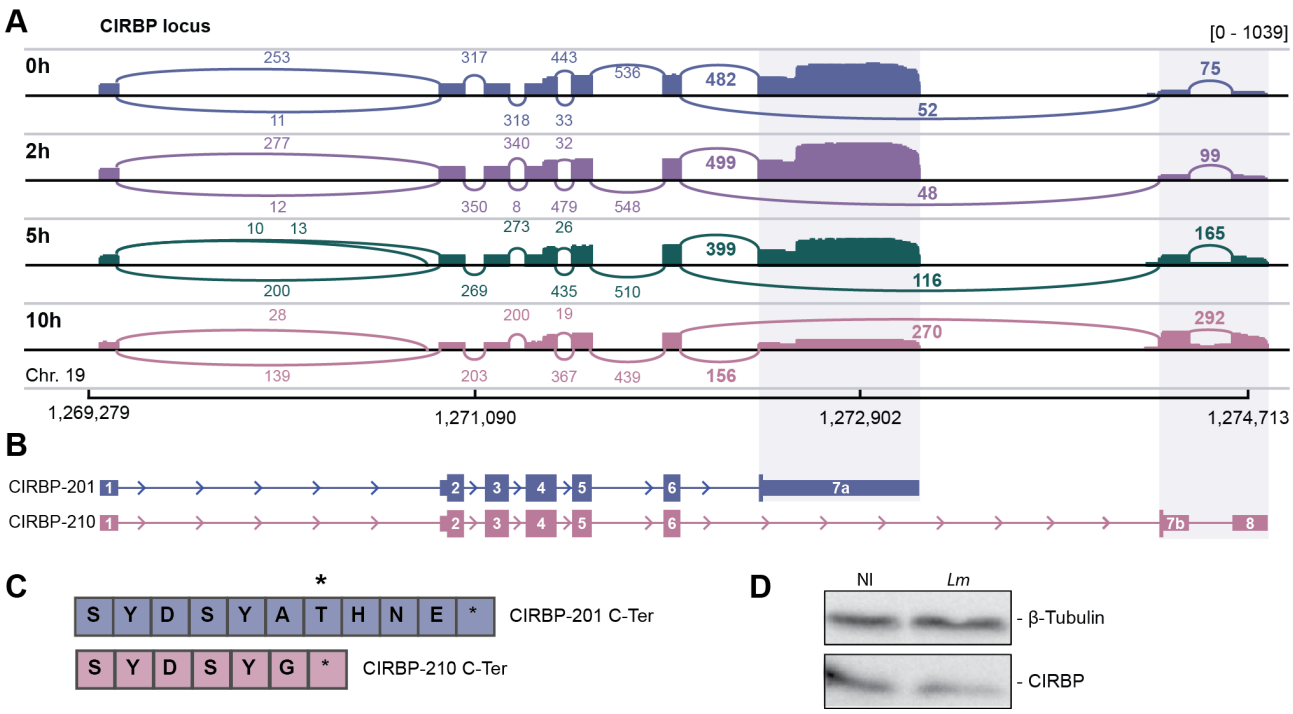

Figure 2. Alternative splicing of CIRBP leads to a switch towards an NMD-sensitive isoform upon *Lm* infection

(A) Sashimi plot of Nanopore sequencing reads aligned at the CIRBP locus. For each timepoint, average values of read counts per genomic position normalized for library size, and exon-junction coverages for each junction, are represented. The range for normalized read counts is indicated between brackets.

(B) Representation of the mature forms of the two prototypical transcripts of CIRBP, CIRBP-201 and CIRBP-210, aligned with their position on the genome in (C). Exons are represented as colored boxes, the height of which is magnified in the CDS; introns are displayed as lines with arrows indicating 5'- to 3'-orientation. Alternative 3'-ends, corresponding to exons 7a in CIRBP-201, and 7b-8 in CIRBP-210, are shaded in pale gray.

(C) Last amino-acids in the sequence of the proteins encoded by CIRBP-201 (*top*) and CIRBP-210 (*bottom*).

(D) Assessment of CIRBP protein abundance by immunoblot on lysates from LoVo cells infected for 10 h with *Lm*, compared to non-infected cells (NI).

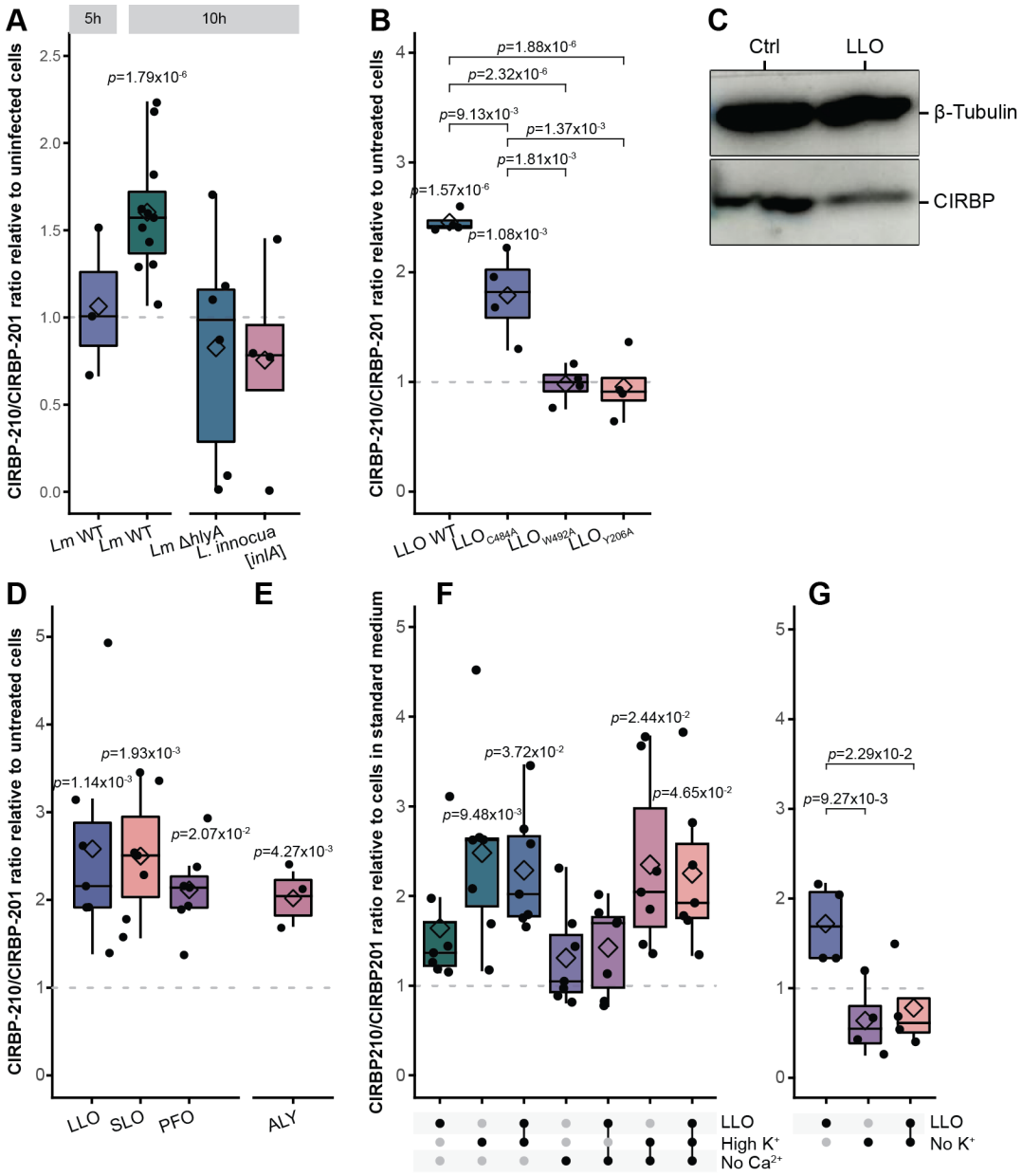

Figure 3. Bacterial pore-forming toxins induce a change in the balance between CIRBP isoforms

(A-B and D-G) Quantification of the relative abundance between CIRBP-210 and -201 transcripts in LoVo cells in response to infection or to exposure to bacterial PFTs. For each condition, the ratio of CIRBP-210 to CIRBP-201 isoforms was quantified by RT-qPCR, and normalized to the CIRBP-210/CIRBP-201 ratio in uninfected, untreated cell (dashed grey lines). Boxplots represent medians and quartiles of data, with the mean represented as diamonds. Two-way ANOVA followed by post-hoc Tukey's test was used for statistical testing between conditions. Each dot represents an independent experiment.

(A) Relative CIRBP transcript ratio in cells infected for 5 h with wild type (WT) *Lm*, or for 10 h with WT *Lm*, with *Lm* deleted for the *hly*A gene (Δ*hlyA*), or with a strain of *L. innocua* rendered invasive by the expression of *Lm* internalin gene *inlA*, compared to uninfected LoVo cells.

825 (B) Relative CIRBP transcript ratio in cells treated for 1 h with 4.5 nm of listeriolysin (LLO) or of catalytically-impaired mutants of LLO, compared to untreated cells.

(C) Assessment of CIRBP protein abundance by immunoblot on lysates from LoVo cells treated for 1 h with 4.5 nM of LLO, compared to untreated cells (Ctrl).

(D-E) Relative CIRBP transcript ratio in cells treated for 1 h with 4.5 nm of CDCs (perfringolysin 830 O, PFO; streptolysin O, SLO) (D), or of aerolysin (ALY) (E), compared to untreated cells.

(F and G) Relative CIRBP transcript expression ratio in cells incubated in isotonic buffers containing varying cation concentrations 30 min, before addition or not of 4.5 nM of LLO for 1 h. (F) Incubation in standard medium containing 140 mM NaCl, 5 mM KCl, 1.5 mM $CaCl_2$, compared with high potassium medium containing 140 mM KCl, 5 mM NaCl, 1.5 mM $CaCl_2$ (High K^+) or 835 calcium-free medium (No Ca^{2+}). (G) Incubation in standard medium, compared with medium lacking extracellular potassium (No K^+).

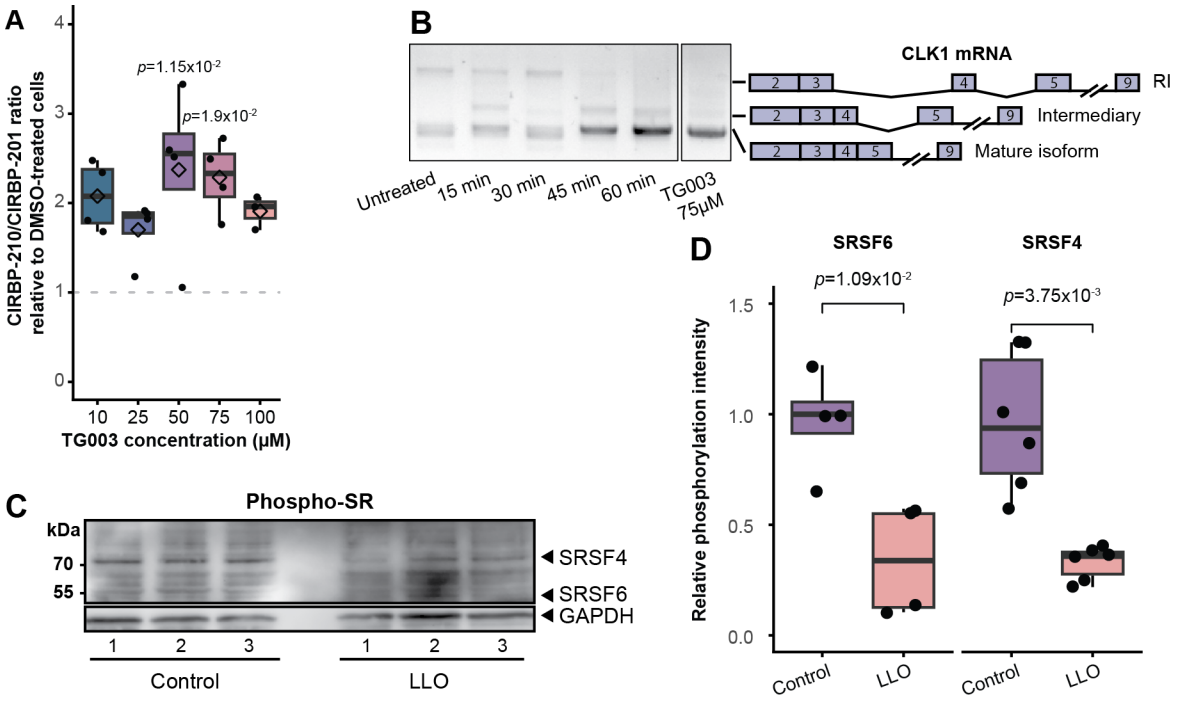

Figure 4. CLK1 activity is regulated in response to LLO-induced stress and impacts CIRBP alternative splicing in LoVo cells

(A) Relative CIRBP transcript ratio in cells incubated for 48 h with increasing concentration of TG003 (n = 3). RT-qPCR quantification was performed and normalized as detailed in the legend to Figure 3.

(B) Assessment of the splicing of CLK1 retained introns 3 and 4 upon incubation with LLO. LoVo cells were treated with 4.5 nM of LLO for 15 min to 1 h, or with 100 μM of TG003, a pharmaceutical inhibitor of CLK1, for 1 h, then the maturation of CLK1 transcripts was assessed by reverse transcription followed by PCR with specific primers.

(C) Assessment by immunoblotting of the phosphorylation status of SR proteins on cells incubated for 1 h with LLO or with TG003 compared to untreated cells (representative experiment).

(D) Quantification of the phosphorylation of SRSF6 and SRSF4 from 4 and 6 independent immunoblots, respectively.

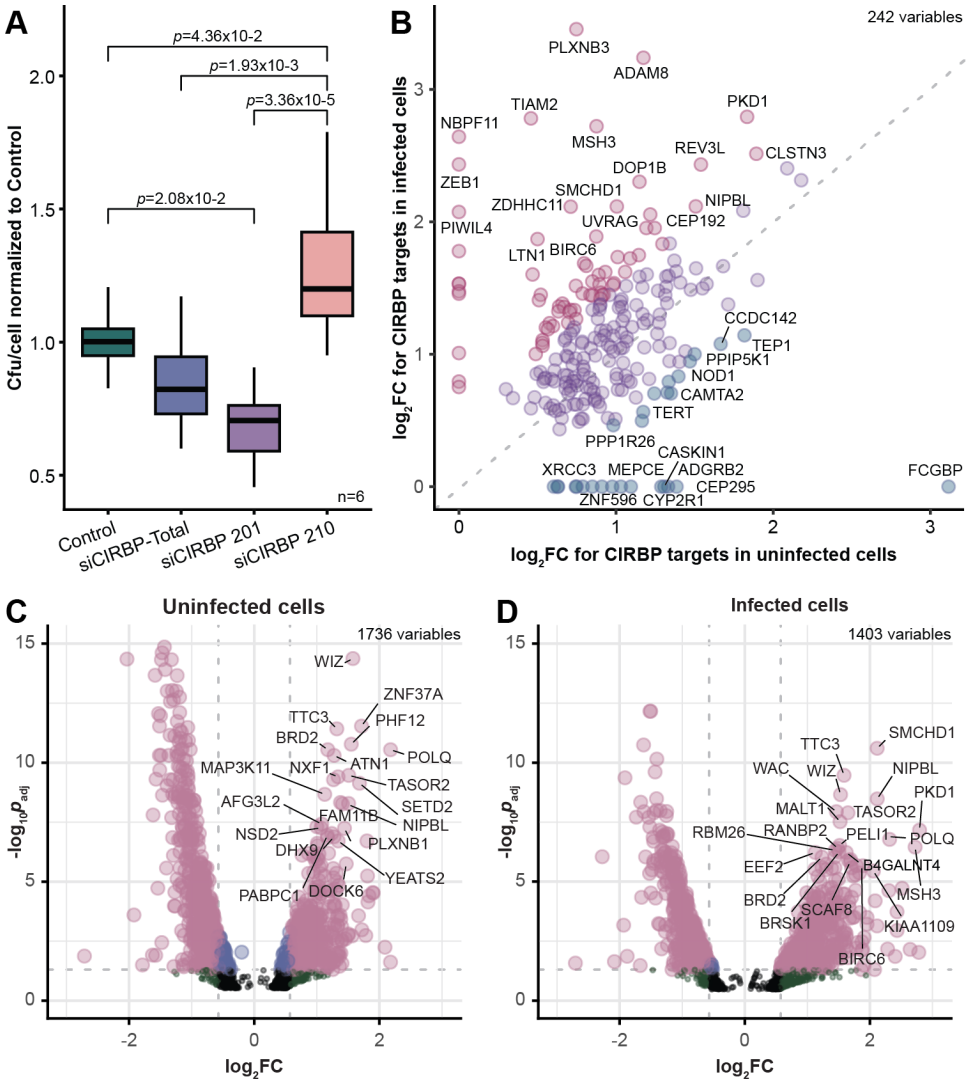

Figure 5. Function of CIRBP in the cellular response to *Lm* infection

(A) Quantification of *Lm* infection in LoVo cells silenced for CIRBP, or for one of its isoforms. Bacterial colonisation of LoVo cells, transfected with siRNA targeting the CIRBP CDS (CIRBP-total), CIRBP-201 3'-UTR, CIRBP-210 3'-UTR or a control scrambled siRNA, was assessed by gentamicin protection assay followed by serial dilution plating of infected cell lysates on agar plates. The number of colony-forming unit (cfu) per cell in each condition was normalized to infection levels in the control condition. One-way ANOVA followed by post-hoc Tukey's test was used for statistical testing between conditions.

(B-D) RNA-immunoprecipitation of CIRBP targets. CIRBP targets were identified by differential expression analysis between a CIRBP-pull down mRNA fraction and both total mRNAs (input) or a control IgG pull-down mRNA fraction. Values of enrichments between the CIRBP pull-down fraction and the IgG pull-down fraction were used for plotting. Pseudogenes were not plotted. Data

865 from two independent replicates. FC, fold change; p_{adj}, adjusted p-value [DESeq false discovery rate (FDR)].

(B) Scatter plots of changes in enrichment of significant CIRBP targets in uninfected *versus Lm*-infected cells. Only transcripts enriched in the CIRBP pull-down fraction in both comparisons (against the input, and against control IgGs) were kept as targets (2,542genes). Data points colored
870 in mauve represent transcripts that were similarly bound by CIRBP in the two datasets ($|\Delta\log_2FC_{Lm\text{-}NI}| < 0.5$), while points colored in pink ($\Delta\log_2FC > 0.5$) and blue ($\Delta\log_2FC < -0.5$) correspond respectively to transcripts enriched in infected and uninfected cells.

(C-D) Volcano plots highlighting CIRBP targets being significantly enriched in (E) uninfected cells and (F) *Lm*-infected cells at 10 hpi compared to the control RIP. Data points colored in pink
875 represent genes with p_{adj} below 0.05 (dashed grey horizontal line, $-\log_{10}p_{adj} = 1.3$) and a FC above 1.5 (vertical dashed grey lines, $\log_2 FC = \pm 0.58$). Grey dots, non-significant; green dots, $\log_2FC > 0.58$, $p_{adj} > 0.05$; blue dots, $p_{adj} < 0.05$, $\log_2FC < 0.58$; pink dots have a $\log_2FC > 0.58$ and a $p_{adj} < 0.05$. The 20 genes with the highest Manhattan distance to the origin were labeled on each graph.

880 # Supplementary material

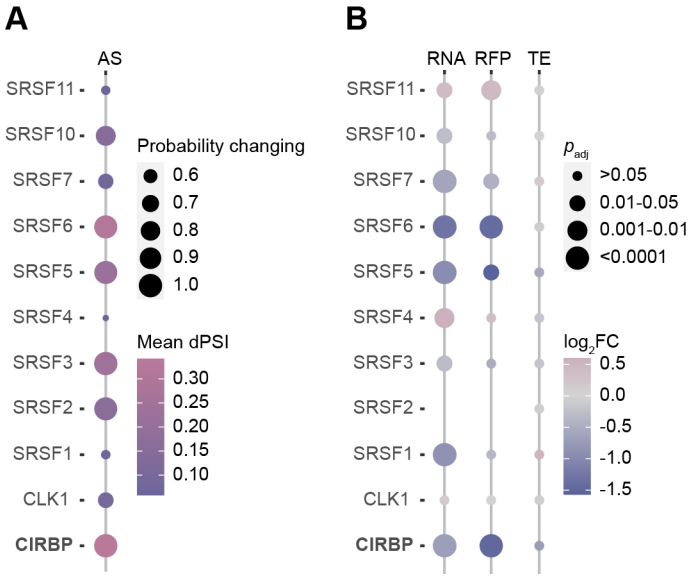

Figure S1. Expression of human genes affected by isoform-based regulations upon 10-h infection with *Listeria monocytogenes*

(A-B) Dot plot highlighting (A) alternative splicing events (dPSI and probability of changing) for
885 a subset of genes of interest at 10 hpi, and (B) their corresponding genes expression in terms of differential mRNA abundance (RNA), ribosomal occupancy (ribosome footprints, RFP) and translation efficiency (TE) when compared to uninfected cells. log_2FC (fold change); p_{adj}, adjusted *p*-value [DESeq false discovery rate (FDR)]. Data from three independent replicates of RNA-seq and Ribo-seq short-read cDNA sequencing.

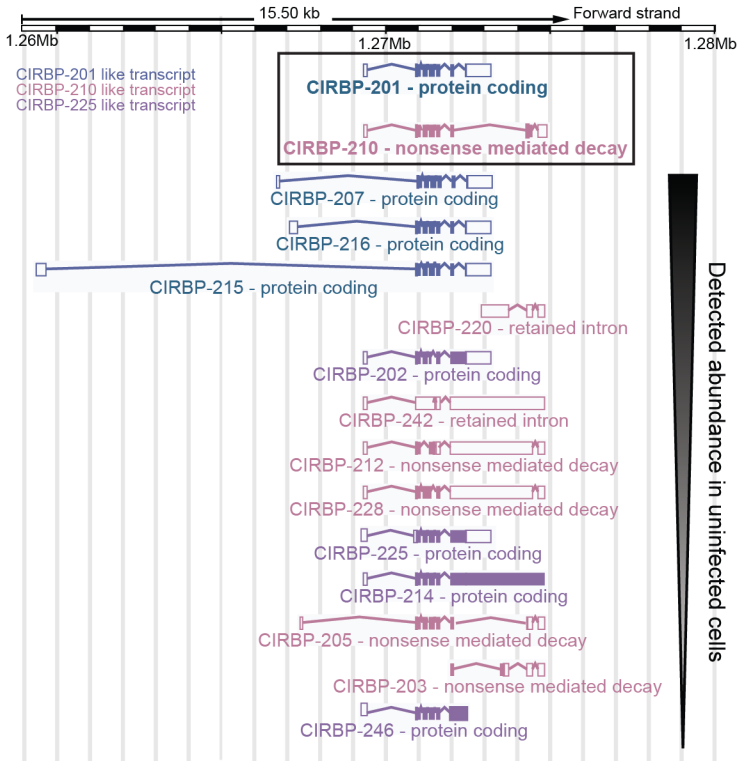

Figure S2. Map of detected CIRBP isoforms in LoVo cells

CIRBP splice variants were grouped into three categories, based on their dominant features. CIRBP-201-like isoforms, displayed in blue, is a dominant class of stable transcripts terminated by exon 7a, and coding for a short version of the CIRBP protein (172 AAs for the prototype version encoded by CIRBP-201). CIRBP-210-like isoforms, in pink, harbor a splice-site between exons 7b and 8 in their 3'-UTR, which make them candidate NMD targets and thus unstable. Most of them encode the short version of CIRBP protein, with only a few amino-acid differences compared with CIRBP-201. CIRBP-225-like transcripts, in purple, encode elongated versions of the CIRBP protein (292 AA for CIRBP-225) and are subdominant in LoVo cells.

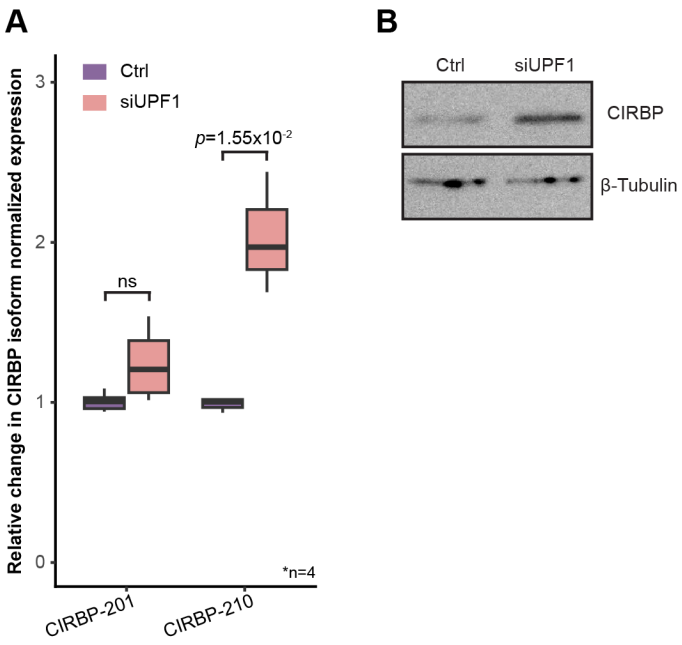

900

Figure S3. CIRBP-210-like transcripts are NMD targets in LoVo cells

(A) Relative CIRBP-210 to -201 transcript ratio in LoVo cells transfected with a siRNA targeting UPF1 (siUPF1) or a control siRNA (Ctrl). RT-qPCR quantification was performed and normalized to levels in the control samples as detailed in the legend to Figure 3.

905 (B) Assessment by immunoblot of CIRBP protein levels in LoVo cells transfected with a siRNA targeting UPF1 (siUPF1) or a control siRNA (Ctrl).

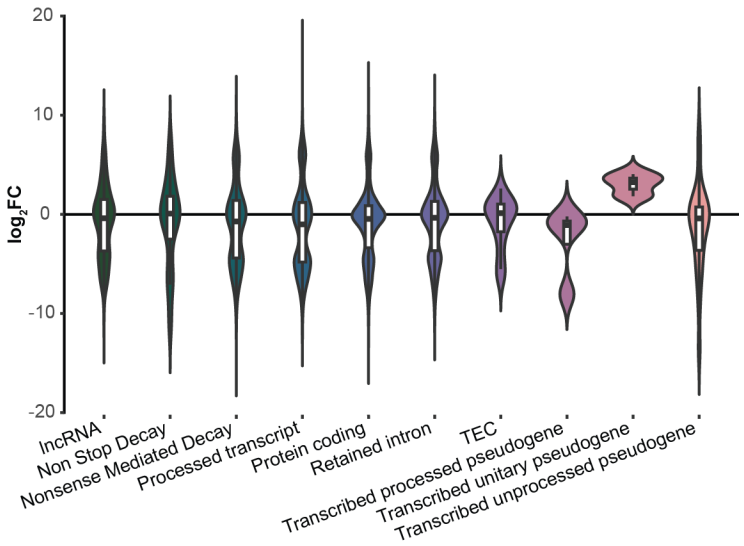

Figure S4. Distribution of isoform switches according to isoform biotypes

910 Violin plot of the $\log_2$ fold change (FC) distribution of the switching isoforms for each isoform biotype represented in BioMart: long non-coding RNA (lncRNA), non-stop decay targets, nonsense mediated decay targets, stable protein coding isoforms, isoforms with a retained intron, so-called "to be experimentally confirmed" (TEC) isoforms, transcribed processed pseudogenes, transcribed unitary pseudogenes and transcribed unprocessed pseudogenes.

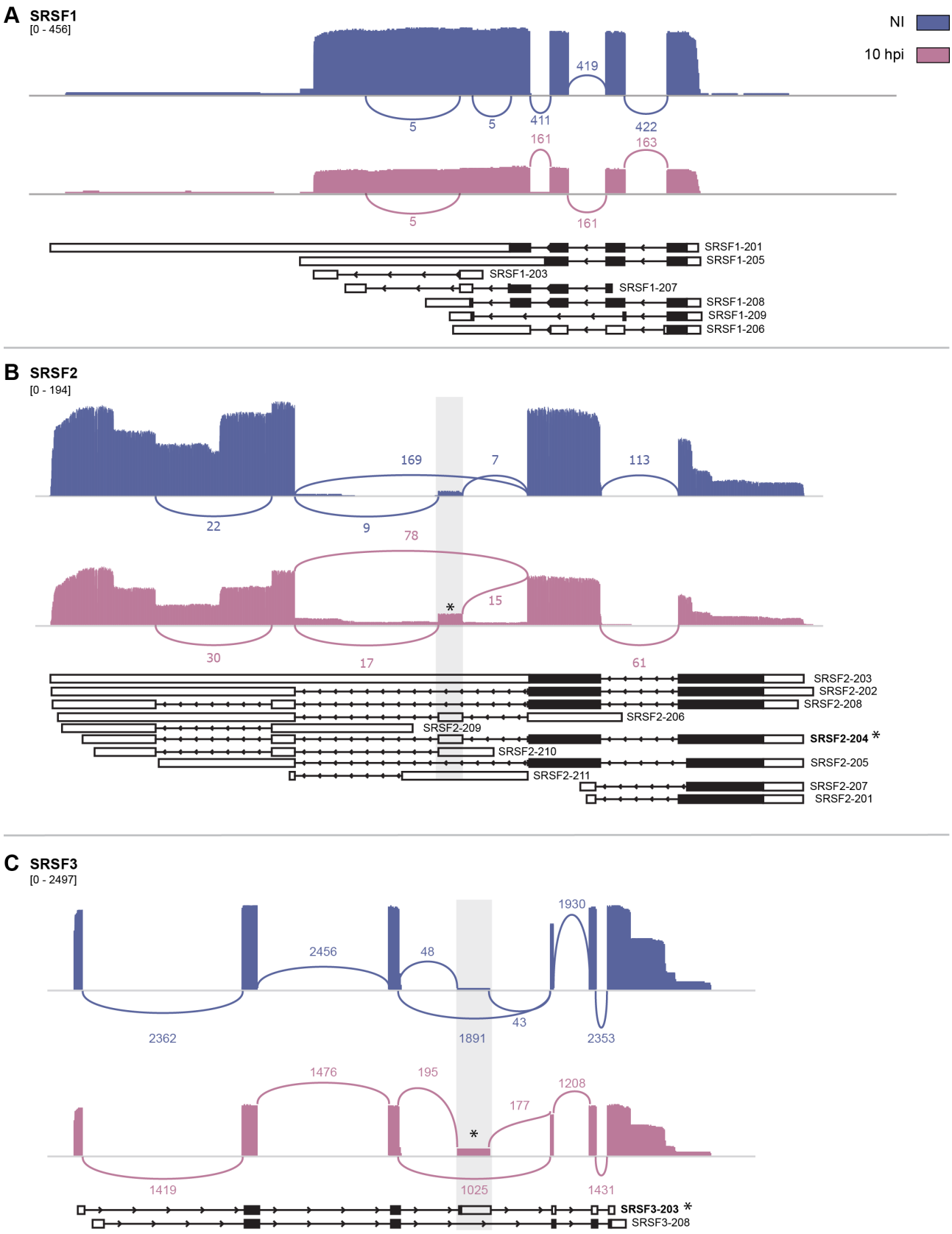
A SRSF1
[0 - 456]
NI
10 hpi
419
5
5
411
422
161
163
5
161
SRSF1-201
SRSF1-205
SRSF1-203
SRSF1-207
SRSF1-208
SRSF1-209
SRSF1-206
B SRSF2
[0 - 194]
169
7
113
22
9
78
15
*
30
17
61
SRSF2-203
SRSF2-202
SRSF2-208
SRSF2-206
SRSF2-209
SRSF2-204 *
SRSF2-210
SRSF2-205
SRSF2-211
SRSF2-207
SRSF2-201
C SRSF3
[0 - 2497]
1930
2456
48
43
2362
1891
2353
1476
195
1208
177
*
1419
1025
1431
SRSF3-203 *
SRSF3-208

915

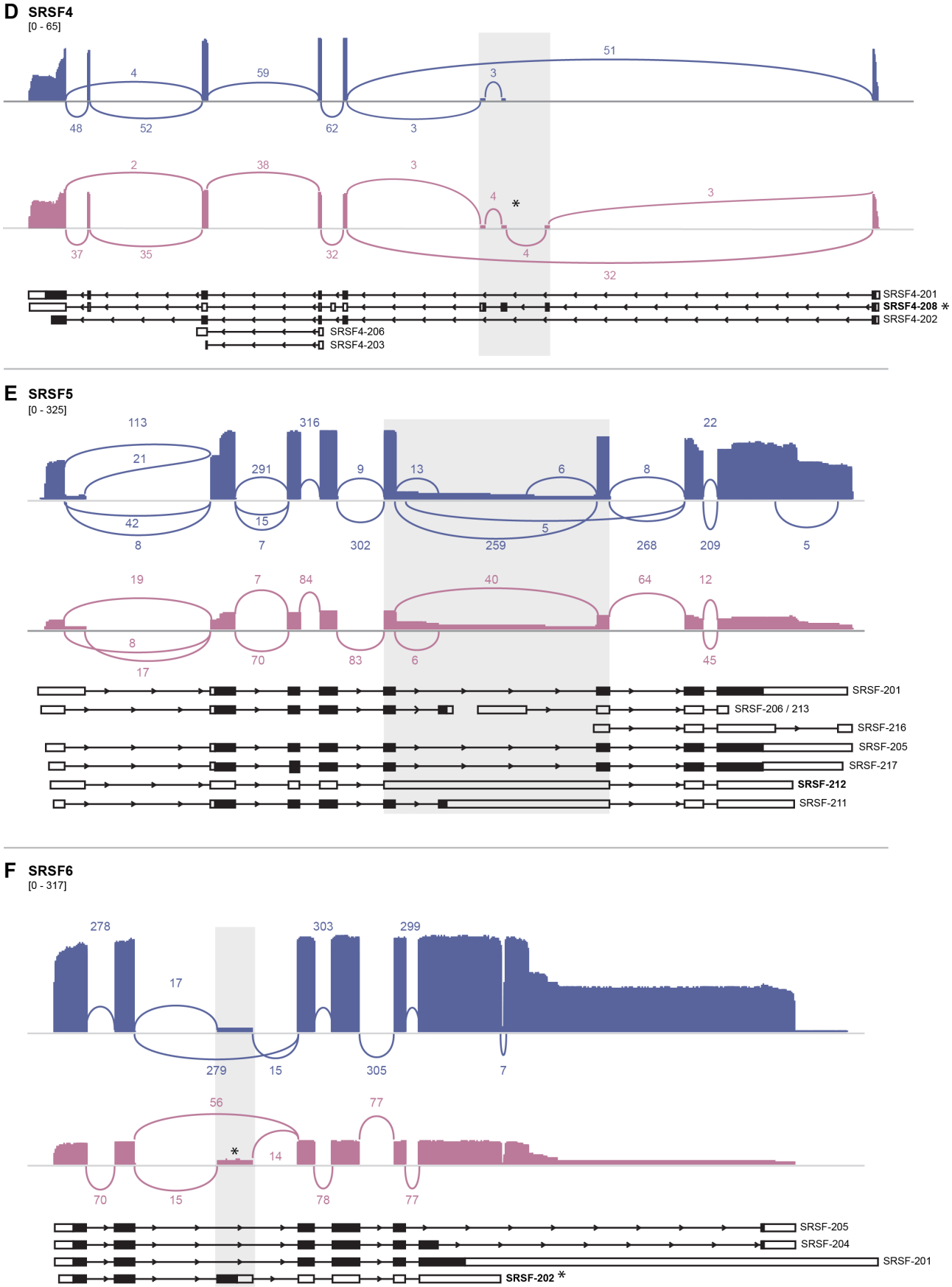
D SRSF4
[0 - 65]
4
59
51
3
48
52
62
3
2
38
3
4
*
3
37
35
32
4
32
SRSF4-201
SRSF4-208 *
SRSF4-202
SRSF4-206
SRSF4-203
E SRSF5
[0 - 325]
113
316
22
21
291
9
13
6
8
42
15
5
8
7
302
259
268
209
5
19
7
84
40
64
12
8
70
83
6
45
17
SRSF-201
SRSF-206 / 213
SRSF-216
SRSF-205
SRSF-217
SRSF-212
SRSF-211
F SRSF6
[0 - 317]
278
303
299
17
279
15
305
7
56
77
*
14
70
15
78
77
SRSF-205
SRSF-204
SRSF-201
SRSF-202 *

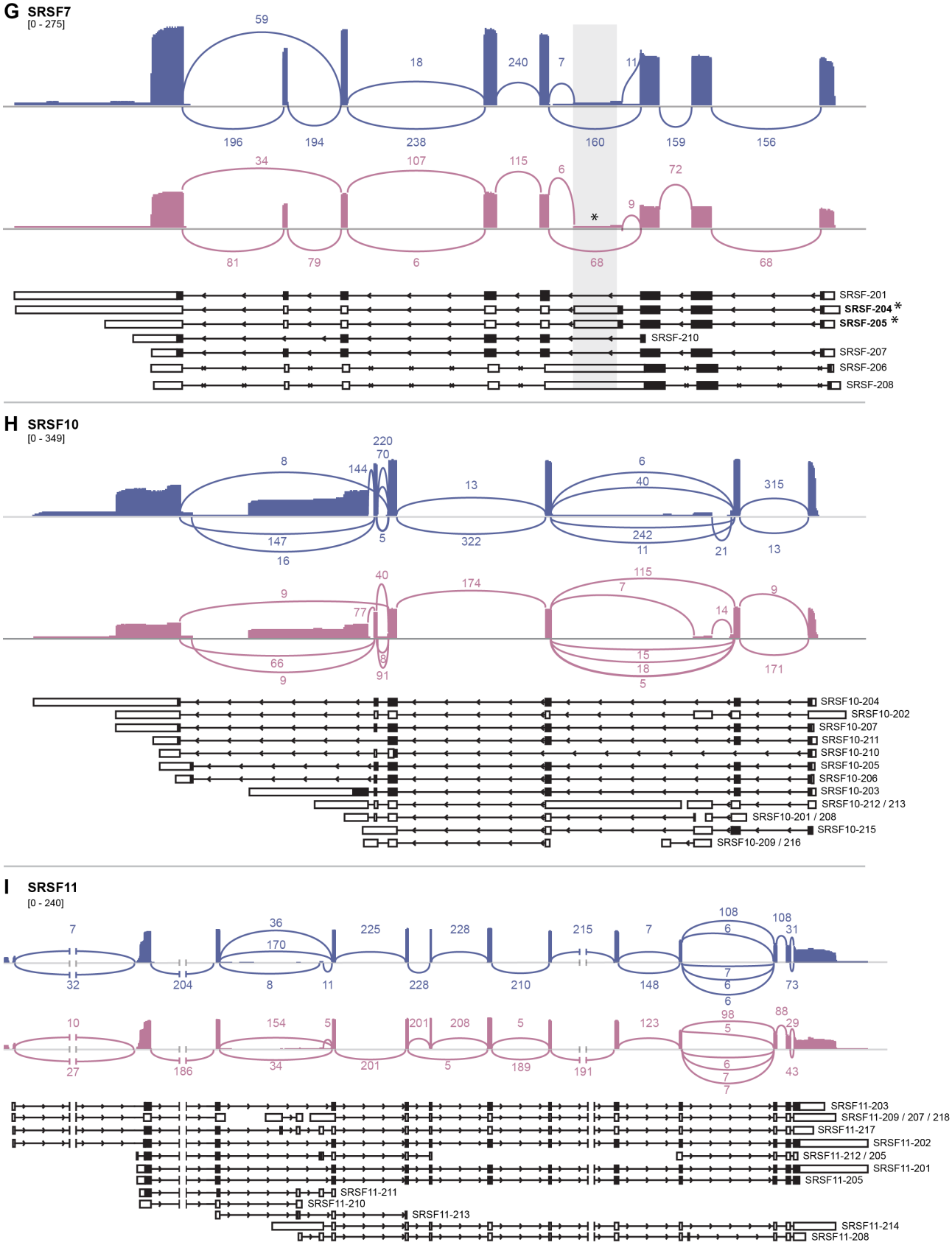
G SRSF7
[0 - 275]
59
18
240
7
11
196
194
238
160
159
156
34
107
115
6
72
9
81
79
6
68
68
SRSF-201
SRSF-204
SRSF-205
SRSF-210
SRSF-207
SRSF-206
SRSF-208
H SRSF10
[0 - 349]
220
70
8
144
13
6
40
315
147
16
5
322
242
11
21
13
40
9
174
115
7
9
77
14
66
9
8
91
15
18
5
171
SRSF10-204
SRSF10-202
SRSF10-207
SRSF10-211
SRSF10-210
SRSF10-205
SRSF10-206
SRSF10-203
SRSF10-212 / 213
SRSF10-201 / 208
SRSF10-215
SRSF10-209 / 216
I SRSF11
[0 - 240]
7
36
170
225
228
215
7
108
6
108
31
32
204
8
11
228
210
148
7
6
73
6
10
154
5
201
208
5
123
98
5
88
29
27
186
34
201
5
189
191
6
7
7
43
SRSF11-203
SRSF11-209 / 207 / 218
SRSF11-217
SRSF11-202
SRSF11-212 / 205
SRSF11-201
SRSF11-205
SRSF11-211
SRSF11-210
SRSF11-213
SRSF11-214
SRSF11-208

Figure S5. Alternative splicing events affect the expression of a subset serine-arginine rich splicing factors (SRSF) upon *Listeria* infection

920 (A-I) Sashimi plots of a subset of SRSF genes, representing exon coverage and exon junctions in uninfected (blue) and *Lm*-infected cells at 10 hpi (pink). Average values of read counts per genomic position normalized for library size, and exon-junction coverages for each junction, are represented. The range for minimum and maximum normalized read counts used as a scale for each SRSF is indicated between brackets, and allows the visualization of overall expression changes between the 925 two conditions. Transcript isoforms identified by mapping long reads to Ensembl annotated transcripts are represented for each gene, with coding sequences displayed as black boxes, and untranslated regions as open boxes. Regions affected by alternative splicing events are highlighted in light grey. Stars indicate the most representative alternative splicing event that led to the inclusion of poison exons (SRSF2, SRSF3, SRSF4, SRSF6 and SRSF7). Other such events occurred, in SRSF1 930 for instance, but were less obviously visualized due to a multiplicity of coexpressed isoforms and to the low stability of transcripts containing poison exons.

Note that isoform attribution is sometimes hampered due to non-exhaustivity of current transcript annotations (see for instance SRSF3-208, the 5'-end of which does not correspond to the transcript that is actually produced in LoVo cells); no corresponding transcript with a matching set of exons is 935 currently available in Ensembl).

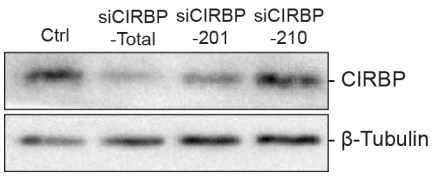

Figure S6. CIRBP protein expression upon CIRBP knock-down

940 Assessment of CIRBP protein expression by immunoblotting in cells transfected by siRNA targeting the common CD domain between CIRBP-201 and CIRBP-210 (siCIRBP-Total), the 3'-UTR of CIRBP-201 specifically (siCIRBP-201) or the 3'UTR of CIRBP-210 specifically (siCIRBP-210). A decrease in CIRBP protein levels was observed upon treatment with siCIRBP-Total and siCIRBP-201, but not with siCIRBP-210, consistently with CIRBP-210 not being expressed in 945 uninfected cells.

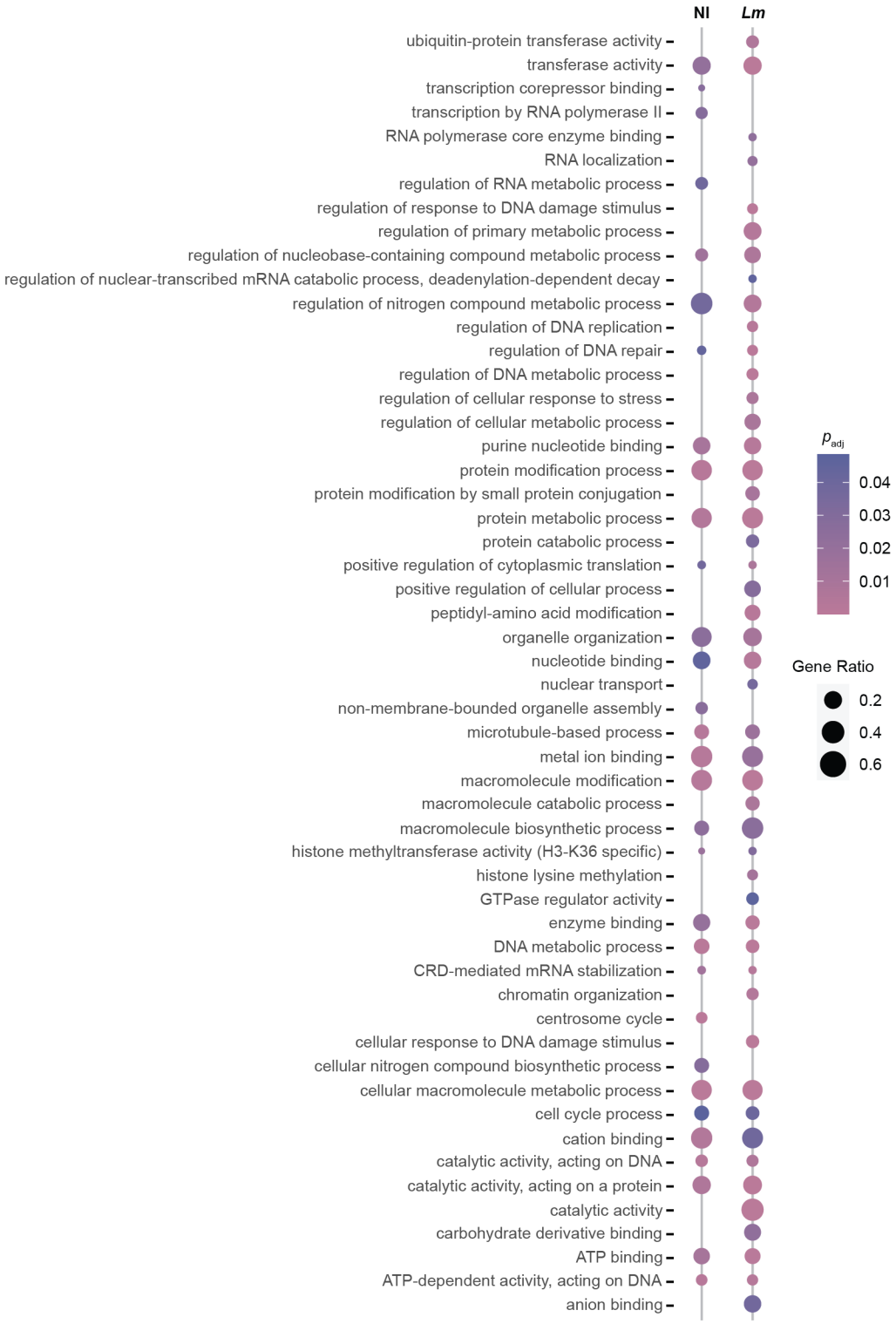

Figure S7. Main biological processes in which products of CIRBP targets are involved

Over-representation analysis (ORA) of GO Biological Process terms for CIRBP targets identified by RIP-seq analysis, either in non-infected (NI) LoVo cells, of at 10 hpi. Only transcripts enriched in the CIRBP RIP when compared by differential expression analysis either to the input, or to control IgGs were kept as targets (223 genes in total). p_{adj}, adjusted p-value.

Table S1. Detection of variations in transcript isoform utilization by Majiq and Bambu-ISAR analysis

(A-C) Output of the majiq algorithm (voila.tsv table) used to detect and quantify alternative splicing events on short read sequencing data, filtered by local splice variant (lsv) with a dpsi > 0.05 at least once. AS events were detected in LoVo cells infected by *Lm* for 2 h (A), 5 h (B) or 10 h (C) compared to non-infected cells and reported as delta in Percent Spliced-In (dPSI) per lsv.

(D-F) Output of the Bambu-ISAR analysis. The R package Bambu was used to detect and quantify transcript variants in long-read data while R package ISAR was used to estimate the difference in usage of these isoforms across two conditions. Outputs give identifying information about the gene and isoform, the variation in both overall gene expression and isoform expression, the fraction of the total gene represented by each isoform in both conditions (IF1 and IF2) and whether a premature termination codon (PTC) is present in the main expressed isoform. This analysis was used to compare isoform switches in LoVo cells infected by *Lm* for 2 h (D), 5 h (E) and 10 h (F) compared to non-infected cells.

(G) Quantification of the representation of each CIRBP class in non-infected cells and cells infected for 10 h by *Lm*. The isoform expression value for each isoform of a given class was summed, then the overall representation of each class was calculated from the total expression for both conditions. The fold-change (FC) values were calculated by dividing the expression value for this class in infected cells by the expression in non-infected cells.

Table S2. CIRBP RIP-seq

(A-D) Output of DESeq2 analyses between the RNA fraction immunoprecipitated by CIRBP and either the input fractions in NI (A) and *Lm*-infected cells (B) or the IgG-immunoprecipitated fraction in NI (C) and *Lm* infected (D) cells. Result for each gene is reported as a log2 fold-change value and its corresponding adjusted *p*-value [p_{adj}, DESeq false discovery rate (FDR)].

Table S3. Bacterial strains used in this study

(A) Bacterial strains used for LoVo cells infections

Strain genotype	Culture medium	MOI	Reference
***L. monocytogenes* LL195**	BHI	30	Weinmaier et al., 2013
***L. innocua* [pGM30-*inlA*(LRRs-IR-SPA)]**	BHI + Cm 7μg/mL	100	Lecuit et al., 1997
L. monocytogenes* LL195 Δ*hlyA	BHI	30	Besic et al., 2020

Columns indicate the identifier of the strain, its species and description, the medium used for growth, the multiplicity of infection used in this study (MOI) used for the infection, and the source reference. BHI, brain heart infusion; Cm, chloramphenicol.

(B) Bacterial strains used for the purification of PFTs

Strain genotype	PFT	Culture medium	Reference
***E. coli* Top10(DE3) [pET29b-LLO-6His]**	LLO	LB + Km (30 μg/ml)	Glomski et al., 2002
***E. coli* Top10 [pET29b-LLO$_{C484A}$-6His]**	LLO$_{C484A}$	LB + Km (30 μg/ml)	Ribet et al., 2010
***E. coli* Top10 [pET29b-LLO$_{W492A}$-6His]**	LLO$_{W492A}$	LB + Km (30 μg/ml)	Ribet et al., 2010
***E. coli* Top10 [pET29b-LLO$_{Y206A}$-6His]**	LLO$_{Y206A}$	LB + Km (30 μg/ml)	Ribet et al., 2010
***E. coli* DH5α [pTrcHisA-PFO]**	PFO	LB + Ap (100 μg/mL)	Farrand et al., 2010
***E. coli* DH5α [pTrcHisA-SLO]**	SLO	LB + Ap (100 μg/mL)	Farrand et al., 2010
***E. coli* NEB5α [pET22b-PA-6His]**	ALY	LB + Ap (100 μg/mL)	Iacovache et al., 2006

Columns indicate the identifier of the strain, its species background and plasmid, the produced PFT, the medium used for culture and the source reference. LB, Luria-Bertani medium; Km, kanamycin; Ap, ampicillin.

Table S4. Oligonucleotides used in this study

(A) siRNA used for gene-specific knockdowns

Identifier	Target	Forward Sequence (5'-> 3')	Reverse Sequence (5'-> 3')
siCIRBP-Total	CIRBP CDS	GUACGGACAGAUCUCUGAAdTdT	UUCAGAGAUCUGUCCGUACdTdT
siCIRBP-201	CIRBP-201 3'UTR	AAAGAUUGUGGGAGCUUCGdCdT	CGAAGCUCCCACAAUCUUUdAdT
siCIRBP-210	CIRBP-210 3'UTR	GACUUCACCUGGAACAAGAdTdT	UCUUGUUCCAGGUGAAGUCdTdT
siUPF1	UPF1	GAUGCAGUUCCGCUCCAUUdTdT	AAUGGAGCGGAACUGCAUCdTdT

Columns indicate siRNA identifier, their target gene and region, their forward and reverse sequences orientated from the 5' end to the 3' end.

(B) Primers for PCR and quantitative PCR

Identifier	Target	Region	Direction	Sequence (5'-> 3')
oAL595	HIF1A	Exon 1	Forward	GAAGTGGCAACTGATGAGCA
oAL596	HIF1A	Exon 2	Reverse	GCGCGAACGACAAGAAA
oAL626	GAPDH	Exon 1	Reverse	CTCTGCTCCTCCTGTTCGAC
oAL625	GADPH	Exon 3	Forward	TTAAAAGCAGCCCTGGTGAC
oAL988	CIRBP	CDs	Forward	CTCAAAGTACGGACAGATCTC
oAL989	CIRBP	CDs	Reverse	TCGTCAATGTTCTCAAAGGTG
oAL990	CIRBP-201	3'UTR	Forward	GACAGTTACGCTACACACAA
oAL991	CIRBP-201	3'UTR	Reverse	CGAAGCTCCCACAATCTTTA
oAL992	CIRBP-210	3'UTR	Forward	GGGTCCTACAGAGACAGTTA
oAL993	CIRBP-210	3'UTR	Reverse	CTCTTGTTCCAGGTGAAGTC
oAL1182	Clk1	Exon1-2 junction	Forward	TGTCCAGGACGATGAGACACTCA
oAL1183	Clk1	Exon 12	Reverse	CATCCCAGTCTAATCGATCGTGG

Columns indicate the primer identifier, the gene ID of the amplified gene, the targeted region, the directionality of the primer and its sequence orientated from the 5' end to the 3' end.